Turbulent bulk transfer coefficients and ozone deposition velocity in ICARTT

C. W. Fairall[1], L. Bariteau[1, 2], A. A. Grachev[1, 2], R. J. Hill[1, 2], D. E. Wolfe[1], W.A.Brewer[1], S. C. Tucker[1,2], J. E. Hare[1, 2, 3], and W. M. Angevine[1,2]

[1]NOAA Earth System Research Laboratory, Boulder, Colorado USA

[2]Cooperative Institute for Research in Environmental Sciences (CIRES), University of Colorado, Boulder, Colorado, USA

[3]SOLAS International Project Office, School of Environmental Sciences, University of East Anglia, Norwich NR47TJ, United Kingdom

Revised for JGR August 30, 2006

Corresponding author: C. W. Fairall, NOAA ESRL R/PSD03, 325 Broadway, Boulder CO 80305-3337, USA. (Chris.Fairall@noaa.gov)

tel: (303) 497-3253 fax: (303) 497-6181

Abstract.

In this paper, we examine observations of shallow, stable boundary-layers in the cool waters of the Gulf of Maine between Cape Cod, MA, and Nova Scotia, obtained in the 2004 New England Air Quality Study (NEAQS-04), which was part of the International Consortium for Atmospheric Research into Transport and Transformation (ICARTT). The observations described herein were made from the NOAA Research Vessel *Ronald H. Brown*. The ship was instrumented for measurements of meteorological, gas-phase and aerosol atmospheric chemistry variables. Meteorological instrumentation included a Doppler lidar, a radar wind profiler, rawinsonde equipment, and a surface flux package. In this study, we focus on direct comparisons of the NEAQS-04 flux observations with the COARE bulk flux algorithm to investigate possible coastal influences on air-sea interactions. We found significant suppression of the transfer coefficients for momentum, sensible heat, and latent heat; the suppression was correlated with lighter winds, more stable surface layers, S-SE wind direction, and lower boundary-layer heights. Analysis of the details shows the suppression is not a measurement, stability correction, or surface wave effect. The correlation with boundary-layer height is consistent with an interpretation that our measurements at 18-m height do not realize the full surface flux in shallow boundary-layers. We also find that a bulk Richardson number threshold of 0.1 gives a better estimate of boundary-layer height than 0.25 or 0.5. Mean ozone deposition velocity is estimated as 0.44 mms^{-1}, corresponding to a boundary removal time scale of about one day.

1. Introduction

According to a study by the Department of Commerce, almost half the population of the United States lives in coastal areas and so is affected by the unique weather and climate of coastal zones [e.g. *Rotunno*, 1994]. Coastal zones are subjectively defined as extending approximately 100 km to either side of the coastline. Examples of coastal meteorological phenomena include the sea breeze, sea-breeze related thunderstorms, coastal fronts, marine stratus, fog and haze, enhanced winter snowstorms, and strong winds associated with coastal orography. For example, the land-sea breeze is produced by the generally different temperatures of the land and sea. The practical application of the coastal meteorology is vital for more accurate prediction of the coastal weather and sea state, which affect defense, transportation, commerce, and pollutant dispersal. The highly variable winds near the coast may sweep pollutants out to sea on a land breeze but then bring them back with the sea breeze [*Rotunno*, 1994].

The transfer of heat, momentum, and water vapor between the atmosphere and the lower surface (over land or over sea) is basic to the coastal meteorology. The atmospheric boundary-layer (ABL) in a coastal zone usually is not horizontally homogeneous and is often associated with nonequilibrium conditions. Over the ocean, the surface drag is determined by the sea state, which in turn may be associated with fetch-limited offshore atmospheric flow. There is another order of complexity over the coastal ocean, because the sea state is significantly influenced by the ocean shelf and shoaling phenomena. Another challenging problem is an internal boundary-layer (IBL) above sea and land. In the coastal waters, advective effects may lead to deviation of flux-gradient relationships from those predicted by Monin-Obukhov similarity theory (MOST) and to violation of the approximation of height-independent flux assumed by MOST.

In July and August 2004, the International Consortium for Atmospheric Research into Transport and Transformation (ICARTT) was the umbrella organization for a large-scale study in the northeastern United States, Canada, and the North Atlantic. The part of that study that focused on regional air quality in northern New England (New Hampshire, Maine, and the Gulf of Maine) was called the New England Air Quality Study (NEAQS-04). The NOAA Research Vessel *Ronald H. Brown* was a key component of NEAQS-04 [*Fehsenfeld et al.*, 2006]. The ship was heavily instrumented for *in situ* measurements of gas-phase and aerosol atmospheric chemistry. Meteorological instrumentation included a Doppler lidar, a radar wind profiler, rawinsonde equipment, and a surface flux package.

The cool waters of the Gulf of Maine cause a shallow stable boundary-layer to form in the summer whenever air flows from the adjacent land. Since the prevailing winds are westerly, these stable boundary-layers are very common in summer. The meteorological instrumentation provided a unique combination of observations to evaluate air-sea transfer processes in the coastal zone with predominantly offshore flow and to contrast those observations with well-established relationships from thousands of hours of open-ocean observations obtained during the last ten years [*Fairall et al.*, 1996a, 2003]. The open-ocean observations formed the basis of version 3.0 of the COARE bulk flux algorithm [*Fairall et al.*, 2003]. In this paper, we report on direct comparisons of the NEAQS-04 flux observations used to investigate possible coastal influences on air-sea interactions. The analysis presented herein emphasizes the mean transfer coefficients in the coastal region. This complements the work of *Angevine et al.* [2006], who provide a more detailed look at boundary-layer profiles and turbulence parameters as they evolve downwind for a few selected cases of offshore flow. More information on the ship track, instrumentation, and an overview of activities can be found in *Fehsenfeld et al.* [2006].

2. Surface-Layer Scaling

Determination and parameterization of momentum, heat, and mass fluxes across the air-sea interface is a central problem in the modeling of the coupled atmosphere-ocean system. Traditional Monin-Obukhov similarity theory (MOST), or surface-layer scaling, is the commonly accepted approach used to describe atmospheric turbulence in the surface layer. This approach is based on the number of assumptions such as a constant-flux layer (shear stress and sensible and latent heat fluxes are approximately constant with height), horizontal homogeneity, temporal stationary etc. It is generally believed that MOST is valid in the marine surface layer as long as turbulent measurements are taken above the wave boundary-layer, WBL [e.g., *Edson and Fairall*, 1998]. In many cases the WBL (the layer where the wave-induced influence cannot be neglected) is typically only of order of O(1 m). However, above-ocean swells the WBL may extend considerably higher during light winds [e.g., *Sullivan et al.*, 2004; *Grachev and Fairall*, 2001; *Sullivan et al.*, 2006].

According to MOST, properly scaled dimensionless characteristics of the turbulence at reference height z are universal functions of a stability parameter, $\zeta \equiv z/L$, defined as the ratio of the reference height z and the Obukhov length scale

$$L = -\frac{u_*^3 \, T_v}{\kappa g\left(\overline{w'\theta'} + 0.61T\overline{w'q'}\right)}, \tag{1}$$

where $u_* = \sqrt{-\overline{w'u'}}$ is the friction velocity, T_v is the virtual air temperature, κ is the von Kármán constant, and g is the acceleration due to gravity. For later use, we define the MOST temperature and humidity scaling parameters $\theta_* = -\overline{w'\theta'}/u_*$, $q_* = -\overline{w'q'}/u_*$.

So-called bulk algorithms to estimate surface air-sea fluxes are widely used in numerical modeling and other important applications. According to this approach, the turbulent fluxes are represented in terms of the bulk meteorological variables of mean wind speed, air and sea surface temperature, and air humidity:

$$\overline{w'x'} = c_x^{1/2} c_d^{1/2} S \Delta X = C_x S \Delta X \,, \tag{2}$$

where *x* can be *u*, *v* wind components, the potential temperature, θ, the water vapor specific humidity, *q*, or some atmospheric trace species mixing ratio. Here c_x is the bulk transfer coefficient for the variable *x* (*d* being used for wind speed) and C_x is the total transfer coefficient. Here ΔX is the sea-air difference in the mean value of *x*, and *S* is the mean wind speed (relative to the ocean surface), which is composed of a magnitude of the mean wind vector part *U* and a gustiness part U_g:

$$\Delta X = X_{sea} - X(z); \qquad S = \sqrt{U^2 + U_g^2} \equiv U\,G\,. \tag{3}$$

Here *z* is the height of measurements of the mean quantity *X*(*z*) above the sea surface (usually 10 m) and $G = \sqrt{1 + (U_g/U)^2}$ is the gustiness factor. The gustiness term in (3) represents the near-surface wind induced by the BL-scale circulations [*Godfrey and Beljaars*, 1991]. In unstable conditions, it is assumed that it is proportional to the *Deardorff* [1970] convective velocity scale

$$U_g = \beta w_* = \beta\left[\left(g/T\right)\left(\overline{w'\theta'} + 0.61T\overline{w'q'}\right)z_i\right]^{1/3}, \tag{4}$$

where z_i is the depth of the convective boundary-layer and $\beta = 1.25$ is an empirical coefficient [*Fairall et al*., 1996a]. Note that (2) with (3)–(4) implies that sensible and latent heat fluxes have a finite limit as U approaches zero. In stable conditions, the COARE algorithm specifies Ug=0.2 ms^{-1}.

The transfer coefficients in (2) have a dependence on surface stability prescribed by MOST:

$$c_x^{1/2}(\zeta) = \frac{c_{xn}^{1/2}}{1-(c_{xn}^{1/2}/\kappa)\Psi_x(\zeta)}, \qquad c_{xn}^{1/2} = \frac{\kappa}{\ln(z/z_{ox})}, \tag{5}$$

where the subscript n refers to neutral ($\zeta = 0$) stability, Ψ_x is an empirical function describing the stability dependence of the mean profile, and z_{ox} is a parameter called the roughness length that characterizes the neutral transfer properties of the surface for the quantity, x (see also *Fairall et al*. [2003] for details). The roughness lengths are specified in Section 6 below.

3. Background on Fluxes in Coastal Regions

A number of important results on the air-sea interaction in coastal zone are based on data obtained during the Risø Air-Sea Experiment (RASEX) at Vindeby, Denmark in 1994 [*Vickers and Mahrt*, 1997, 1999; *Mahrt et al*. 1998; *Mahrt*, 1999]. In RASEX the flux measurements were made at a tower located 2 km off the northwest coast of the island of Lolland in shallow water (~ 4 m average depth). Eddy correlation fluxes of momentum and virtual temperature were calculated from sonic anemometers at four levels located at 6, 10, 18, and 32 m above the mean sea level. However, the studies of *Vickers and Mahrt* [1997] and *Mahrt et al.* [1998] used flux data only from the 10 m sonic (Gill/Solent). Compared to the open-ocean situations, the RASEX data are characterized by fetch-limited conditions. Local offshore flow conditions are characterized by a sea fetch ranging between 2 km and 5 km. Onshore flow has a fetch between 15 km and 25 km. The nearby land surface is relatively flat. The observation period is also characterized by a near absence of large amplitude swell. Both stable and unstable stratifications in the ABL have been observed during RASEX.

According to *Vickers and Mahrt* [1997] variation of the neutral drag coefficient in RASEX is dominated by variation of wave age, frequency bandwidth of the wave spectra, and wind speed. For a given wind speed, the drag coefficient is larger during conditions of short-fetch (2–5 km) offshore flow with younger growing waves than it is for longer-fetch (15–25 km) onshore flow. This is consistent with the concept of enhanced wind stress over younger growing waves compared to older wave fields, which are more in equilibrium with the wind [e.g., *Kitaigorodskii*, 1970; *Snyder et al*., 1981; *Geernaert et al.*, 1987; *Smith et al*., 1992; *Donelan et al*., 1993]. For the strongest onshore winds, wave breaking enhances the drag coefficient. Using the RASEX data, *Vickers and Mahrt* [1997] developed simple models of the drag coefficient and roughness length in terms of wind speed, wave age, and bandwidth. An offshore flow model of the drag coefficient in terms of nondimensional fetch is developed for situations when the wave state is not known.

Vickers and Mahrt [1999] used RASEX data to study the nondimensional wind shear, φ_m, in the coastal zone. They found that the development of shallow internal boundary-layers and young, growing wave fields, both of which are common in the coastal zone, can lead to substantial departures of the nondimensional shear from the MOST prediction based only on stability. For example, the largest-scale turbulent eddies are suppressed in shallow convective internal boundary-layers, leading to larger φ_m than that of the traditional MOST prediction. In shallow stable boundary-layers, elevated generation of turbulence leads to smaller nondimensional shear compared to the traditional prediction. Above young, growing waves in stable stratification, the observed φ_m is less than that above older, more mature waves in otherwise similar conditions. Based on the RASEX data for all the onshore and offshore flow periods, *Vickers and Mahrt* [1999] proposed a new general formulation for φ_m in coastal zones as a function of the traditional stability parameter and IBL depth for the unstable cases (their Equation [9]), and as a function of the stability parameter and wave state for the stable cases (their Equation (10)).

Mahrt et al. [1998] found for the RASEX coastal zone data that the thermal roughness length shows no well-defined relation to the momentum roughness length or roughness Reynolds number, in contrast to previous theories. In fact, the two roughness lengths are governed by different physics. The variation of the momentum roughness length for this data set is dominated by the wave state and, in contrast to thermal roughness, increases at weak winds [see *Vickers and Mahrt*, 1997]. The thermal roughness length shows significant dependence on the wave state only for small values of wave age where the mixing is apparently enhanced by wave breaking. On the other hand, the thermal roughness length is more related to the occurrence of internal boundary layers. The development of thin IBLs with offshore flow substantially reduces the heat transfer and thermal roughness length but has no obvious influence on momentum roughness length. The RASEX data indicate that the internal boundary-layer effect is more significant for unstable conditions compared to stable conditions. Suppression of large efficient transporting eddies by the low boundary-layer top is one of several plausible explanations for the reduced heat flux. A new formulation of the thermal roughness length based on the internal boundary-layer depth is calibrated to the RASEX data. The relationship between the thermal roughness length and the internal boundary-layer depth breaks down in the very stable case where the boundary-layer is characterized by an upside-down structure, with the generation of turbulence occurring mainly detached from the surface.

The RASEX offshore flow drag coefficients reported by *Vickers and Mahrt* [1997] agree reasonably well with those reported by *Donelan* [1982] from data collected near the coast of Lake Ontario, Canada, and reported by *Smith et al.* [1992] for young growing waves. However, both the data of *Rieder* [1997] and the model of *Geernaert et. al.* [1987] suggest significantly larger drag coefficients for a given wave age than those observed in RASEX.

Mahrt et al. [2001] and *Sun et al*. [2001] studied spatial variations of the surface stress over a coastal shoaling zone offshore of Duck, North California, using the LongEZ research aircraft. Data were obtained in 1997 and 1999 during the Shoaling Wave Experiment (SHOWEX). *Sun et al*. [2001] reported that the spatial variation of the friction velocity with offshore distance is much larger with offshore flow than with onshore flow. With onshore flow the friction velocity is strongly correlated with surface waves. However, for the offshore flow cases, the friction velocity decreases rapidly with offshore distance for the first several kilometers. As a result of the influence of the upstream land surface, the neutral drag coefficient is not correlated with the atmospheric bulk Richardson number for the first 5 km off the coast. *Mahrt et al.* [2001] found that with offshore flow of warm air over cold water, stability restricts momentum transfer to the waves, and the aerodynamic surface roughness decreases to very small values, which in turn decreases turbulent mixing. The structure of the offshore flow in these measurements can be found in *Vickers et al*. [2001].

There have been few detailed measurements of the stable IBLs over oceans [e.g., *Garratt*, 1987; *Garratt and Ryan*, 1989; *Friehe et al*. 1991; *Smedman et al*. 1997]. *Garratt* [1990] reviewed IBLs. *Rogers et al*. [1995] discussed the general structure of a stable IBL that forms over the sea, downstream of a warm landmass based on aircraft measurements from the Internal Boundary Layer Experiment (IBLEX) conducted over the Irish Sea in 1990. They found that, despite the large horizontal inhomogeneity in the IBL, local similarity scaling applies throughout the IBL below the local similarity length scale. The local similarity length scale is the local Obukhov length based on the local fluxes at height z rather than on the surface values as defined by Nieuwstadt (1984). Thus, the height *z* remains an important scaling parameter. The turbulence parameters, which are nondimensionalized with the local scales, are generally constant with respect to height. However, near the top of the IBL, dependence on *z* disappears because the surface does not affect the turbulence. The IBL is characterized by large temperature and moisture gradients and a large wind shear that maintains a Richardson number close to its critical value. Turbulence appears to be continuous, maintained by the strong wind shear against the stabilizing effect of the downward-directed heat flux. A long fetch, the designation of an IBL becomes tenuous especially after the turbulent structure of the original BL has decayed or been consumed by the IBL. For stable IBLs formed below an convection BL generated over land, the mean thermal structure of the old BL changes slowly while the wind profile may change significantly. The distinction between and IBL and an new 'equilibrium' BL is unclear and we will use the terms interchangeably.

For the case of warm air advected over cold water, *Garratt* [1990] showed that close to shore the IBL depth h can be estimated by

$$h = \alpha^{1/2} U (\frac{g\Delta\theta}{\theta})^{-1/2} x^{1/2} = \alpha Ri_b^{-1} x , \quad (6)$$

where $\alpha^{1/2}$=0.02 and Ri_b is a bulk Richardson number defined by the flow properties incident at the coast

$$Ri_b = \frac{gh(\theta_v - \theta_{vs})}{\theta_v U^2} , \quad (7)$$

wherein θ_v and U are the atmospheric mixed-layer properties over land that flow out onto the sea with surface virtual potential temperature θ_{vs}. *Skyllingstad et al*. [2005] did modeling studies for offshore flow onto cold water (5 K cooler than the incident boundary-layer) and found turbulent kinetic energy and surface stress dropping rapidly within a few km of shore. Their results show the boundary-layer cooled less than 1 K at 4 km fetch with a stable surface layer about 20 m thick. See also *Angevine et al*. [2006] for more discussion of IBL depth in NEAQS-04.

4. Observation Systems

4.1. Turbulence and Bulk Meteorology

NOAA's Earth System Research Laboratory (ESRL: formerly the Environmental Technology Laboratory, ETL) sea-going flux and meteorology measurement system was fully described in *Fairall et al*. [1997, 2003]. The following deals with specific aspects of that measurement system that are relevant to computing bulk transfer coefficients. The basic measurements used in this paper are covariance and inertial-dissipation (ID) turbulent flux estimates, combined with measurements of the basic bulk variables as described in section 2. A sonic anemometer (Gill/INUSA RS-2A) is used to obtain the three components of the wind vector (u', v', w') and the sonic temperature (T'). Two high-speed infrared hygrometers (Ophir Corporation IR-2000 and LiCOR LI7500) are used to obtain q'. Velocity fluctuations in fixed-earth coordinates are obtained from the raw anemometer output by applying rotations to account for pitch, roll, and yaw plus corrections for the ship's velocity vector. High-frequency (i.e., surface wave-induced) motions are measured with an integrated package of angular rate sensors and accelerometers (Systron Donner Motionpak) which forms the mounting base of the sonic anemometer. Lower-frequency motions are obtained from a Global Positioning System (GPS), a gyrocompass, and the ship's Doppler speed log. Details of the motion correction are given in *Edson et al*. [1998]. Sonic temperature is corrected for velocity crosstalk and the humidity contribution, as discussed in *Fairall et al*. [1997]. ID flux estimates are computed from the variance spectral density of u', T', and q' in the inertial-subrange of locally isotropic turbulence, also as described in *Fairall et al*. [1997]. The ID range is usually at frequencies sufficiently above the wave-induced platform motions, so corrections are not needed.

The optics of the high-speed hygrometers can be contaminated by salt [*Fairall* *and Young*, 1991; *Fairall et al*., 1997] and require daily cleaning. Data obtained with water on the optics (e.g. during rainfall or fog) ar unreliable and, in some conditions, sunlight also invalidates the measurement. The condition of the optics is monitored in the data stream and a threshold is set to reject such data. Because of these three sources of error, usable data for latent heat flux are significantly less than for stress.

Mean wind speed and mean vector wind magnitude are obtained from the sonic anemometer after transformation to fixed-earth coordinates. The relative wind vector is first corrected for distortion by the ship using results from computational flow dynamics calculations. A floating thermistor is used to obtain a near-surface value for the ocean temperature (the depth is about 5 cm). The COARE cool-skin algorithm [*Fairall et al*. 1996b] is used to obtain the interface temperature, which is typically 0.3 C cooler than the bulk temperature. Mean air temperature and humidity are obtained with a combined temperature/relative humidity (RH) sensor in an aspirated radiation shield (Vaisala HMP-235 with 0.1 C, 2% RH quoted accuracy).

Covariance and ID fluxes and mean variables are computed in 10-min chunks from a nominally 1-hr time section and then averaged to 1-hr. A coordinate rotation of the high-speed time series is performed on the mean earth-fixed velocity vector, following *Tanner and Thurtell* [1969] to produce streamwise coordinates for the 1-hr period. The 10-min covariance and ID fluxes were selected for quality criteria and those that pass are averaged in 1-hr blocks.

Covariance flux estimates are subject to random sampling errors associated with atmospheric variability [*Finkelstein and Sims*, 2001] and other random errors caused by imperfect motion corrections or sensor noise and drift. Systematic errors are caused by incorrect sensor calibration, imperfect motion correction, and flow distortion. For well-placed sensors on ships, flow distortion is a serious concern only for stress. We have applied no empirical distortion correction to our covariance data but note a possible systematic uncertainty of about 10% for stress. The absolute accuracy of transfer coefficient measurements is subject to uncertainties in the mean measurements, the fluxes, and in the case of neutral transfer coefficients (or roughness length), the MOST stability functions.

4.2. Profiling

The profiling systems used on the R/V *Ronald H. Brown* during NEAQS-04 were described by *Wolfe et al.* [2006], so only a brief summary is presented here. Three primary sensors, namely, two remote sensors and one *in situ* sensor, were used to measure wind profiles. Rawinsondes using GPS wind tracking were launched four to six times daily, providing a detailed profile of winds. A radar wind profiler (RWP) permanently deployed on the ship and corrected in real-time for ship motion, provided continuous hourly profiles at 60- and 100-m vertical resolutions. A High Resolution Doppler LIDAR (HRDL) with a 30-m along-beam resolution was operated during the experiment by ESRL. The rawinsonde system used Vaisala RS-92 digital sondes which also measured profiles of temperature and relative humidity.

The Doppler lidar is an active remote sensing system with hemispheric scanning capability, similar in many respects to the more familiar Doppler weather radar, except it transmits in the near infrared (2.02 μm) instead of radio-frequency waves. The scattering targets for shorter-wavelength lidar are atmospheric dust and/or aerosol particles, which are ubiquitous in the lower troposphere and allow the lidar to obtain signal in cloud- and precipitation-free air. Data from the lidar can include aerosol *backscatter,* which is related in a complex way to aerosol concentration (and other aerosol properties), and *frequency*, from which the Doppler velocity component is calculated. The lidar's scanning strategy during NEAQS-04 included sweeps along both constant azimuth and elevation angles to provide a variety of high-resolution boundary-layer information. Azimuth scanning produces cones of data which, at the lowest elevation angles, can provide surface wind data and elevation scanning, and which, at the highest elevation angles, can produce vertical slices of atmospheric features. The 360° azimuth scans, usually completed in 2 min or less, were processed to produce vertical profiles of the horizontal wind using the velocity-azimuth display (VAD) technique.

5. Boundary-layer Profiles

Rawinsondes were launched at 6 hour intervals from the ship's stern. For all 123 sondes, profiles from the surface to 260 m were prepared for analysis of the near-surface meteorology. A plethora of near-surface cases was observed; only a few examples can be shown here. More examples can be found at (ftp://ftp.etl.noaa.gov/et6/archive/NEAQS_2004/RHB/Scientific_analysis/lowheights). Wind speed varied from calm to about 15 m/s. Wind directions at 17.5 m and 250 m varied from parallel to opposite and in all directions. Sea colder than the air resulting in near-surface stability was typical, but sea warmer than the air resulting in shallow convective instability was also observed.

Figure 1 shows the position of four sample rawinsonde launches relative to the coastline at UTC shown as year, month, day, hour, minute (yy mm dd hh mm) in the titles. The red and black arrows in Figure 1 show the wind vector at 17.5 m (sonic anemometer) and at 250 m (sonde), respectively. One degree of longitude corresponds to 3 m/s. The four cases in Figure 1 are labeled (a) to (d). Figures 2a–d show the corresponding profiles for cases (a) to (d), and show latitude (lat), longitude (lon), UTC (yymmddhhmm), and UTC Julian day (JD). Ten-minute averaged data from the sonic anemometer at 17.5 m height, temperature and humidity at 15.5 m, and sea-surface temperature as well as 15-minute averaged lidar data are included on the profiles when those averages exist within one half hour of the rawinsonde launch. Wind speed (m/s) and direction in degrees are shown for the sonde (blue), lidar (green), and sonic anemometer (red). Differences between lidar and sonde data at the lowest heights is likely because the sonde is launched in the ship's air wake, whereas discrepancies can be caused at greater heights by temporal mismatch. The potential temperature (green) and virtual potential temperature (blue) in Kelvin and water vapor mixing ratio in g/km (blue) are obtained from sonde data; those quantities are shown as obtained from ship instrumentation at 15.5 m (red) and at the surface (red). For calculation of surface values, it is assumed that water vapor is saturated at the sea surface temperature. The lidar velocity variance in $m^2\ s^{-2}$ is obtained from the lidar velocity signal in m/s after the mean velocity is removed; thus, lidar velocity variance contains atmospheric waves and turbulence and instrumental noise. Calculation of the gradient Richardson number (*Ri*) in the figures requires the ratio of the potential temperature gradient to the sum of the squares of the gradients of the horizontal wind components; as such, it is sensitive to errors. The bulk Richardson number is referenced to the surface values; that is, it requires the difference of potential temperature aloft to its surface value divided by the square of the wind speed aloft. The bulk Richardson number is shown on two scales. Vertical lines corresponding to gradient $Ri = 0.25$ and to bulk $Ri = 0.1$, 0.25, and 0.5 are shown. Richardson number calculated entirely from sonde data is in blue, whereas substitution of lidar velocity data in place of sonde velocity data produces Ri as shown in green.

Figure 2a and corresponding case (a) in Figure 1 show that wind at 250 m is offshore from Boston, but near-surface flow is toward Maine. In Figure 2a, the sea is colder than the air, and the largest gradients of both water vapor mixing ratio and potential temperatures are between 40 and 75 m. In that height range, the gradient Ri shows a stable layer where lidar velocity variance is enhanced, which suggests that atmospheric waves are present. Conditions for shear-generated turbulence exist above and below the stable layer. Most of the shear aloft is caused by change of wind direction.

Figure 2b corresponds to case (b) in Fig. 1. Flow is offshore at 250 m, but onshore at 17.5 m. Light wind causes discrepancy of the sonde’s wind direction and speed at low levels relative to the lidar and sonic anemometer data. However, it is clear from agreement of lidar and sonde data that wind speed almost vanishes from 150 m to 200 m, and that there is a large wind-direction shift between those heights. The sea is warmer than the air, but the potential temperature gradient reverses at about 40 m. The Richardson numbers indicate convective instability below about 40 m, but stability above

50 m. Enhanced lidar variance between 50 and 110 m might indicate atmospheric wave activity.

Case (c) in Figure 1 shows that wind at the height of 250 m is from the direction of Boston, but nearer-surface flow is toward the coast of Maine. Corresponding Figure 2c shows sea temperature substantially colder than the air at 17.5 m, and the potential temperature profiles show strong gradients up to 110 m, above which the potential temperatures are constant. The Richardson numbers indicate shear-generated turbulence, despite the thermal stability, from the surface to about 70 m, above which the flow stabilizes. A small enhancement of lidar velocity variance is seen between 50 and 100 m. Profiles of stability and lidar velocity variance suggest the presence of atmospheric waves, perhaps breaking waves.

Figure 2d and case (d) in Figure 1 show a case of strong wind at 250 m which is offshore from Massachusetts. Wind speed at 17.5 m is toward Maine and of smaller speed than aloft. The sea is colder than the air. The Richardson numbers suggest turbulence below 140 m, which is corroborated by the enhanced lidar velocity variance, and suggest stability above 140 m. Wind shear is strongest below 140 m. Between 140 to 150 m, there are enhanced gradients in potential temperatures and water vapor mixing ratio.

6. Transfer Coefficients

6.1. Methods

The reduction of an ensemble of observations of turbulent fluxes and near-surface bulk meteorological variables to estimates of the mean 10-m neutral transfer coefficient is a problem of some subtlety. The straightforward approach is to convert each observation to C_{x10n}

$$C_{x10n} = \frac{\overline{w'x'}}{U_{10n}\Delta X_{10n}G}, \tag{8}$$

then average to obtain

$$< C_{x10n} >=< \frac{\overline{w'x'}}{U_{10n}\Delta X_{10n}G} > . \tag{9}$$

The 10-m neutral values of the mean profile are computed as

$$U_{10n} = \frac{u_*}{\kappa}\ln(\frac{10}{z_o}) = U(z) - \frac{u_*}{\kappa}[\ln(\frac{z}{10}) - \Psi_u(z/L)] \tag{10a}$$

$$\Delta X_{10n} = -\frac{x_*}{\kappa}\ln(\frac{10}{z_{ox}}) = \Delta X(z) + \frac{x_*}{\kappa}[\ln(\frac{z}{10}) - \Psi_q(z/L)] , \tag{10b}$$

where x_* can be θ_* or q_*. Note, the sign difference between [10a] and [10b] follows from ΔX being defined as $X_s - X(z)$ in Equation [3]. However, artificial correlation may confuse the results. In this paper, we use the approach of *Fairall et al*. [2003] to compute estimates of the mean transfer coefficients as a function of wind speed. Here the fluxes are averaged in wind speed bins and the mean transfer coefficient is the one that correctly returns the mean or median flux

$$< C_{x10n} >= \frac{< \overline{w'x'} >}{< w'x' >_b} < C_{x10nb} >, \tag{11}$$

where the subscript *b* refers to values computed with the bulk algorithm.

The data used in the analysis are filtered for acceptable relative wind direction and other data quality criteria described by *Fairall et al*. [2003].The results for momentum and sensible heat flux are shown in Figures 3a and 3b. Comparison with the COARE algorithm coefficients shows substantially lower transfer with decreasing wind speed for both sensible heat and momentum. Similar behavior occurs for latent heat flux, but the number of usable observations is lower and less convincing (not shown).

6.2. Analysis

The substantially reduced transfer coefficients (or, equivalently, fluxes) at low winds are perplexing. It might be a measurement problem, a stability correction issue, an ocean surface wave effect, or an atmospheric internal boundary-layer process. The most obvious reason for a measurement problem is inadequate motion compensation for covariance fluxes. This usually produces a peak in the *w-u* or *w-T* cospectra at the dominant wave period. Figures 4a and 4b show sample *w-x* cospectra for *U*, *T*, and *q* for two periods. It is clear that the cospectra are very clean and free of wave effects (i.e., no anomalous peaks near 0.2 Hz). Also, the cospectra approach zero well below the Nyquist frequency so that fluxes are not underestimated. That is, the high-frequency contributions are well resolved. Of course, wind mean speed may not be the ideal variable to discern the physics of this behavior. In Figure 5 we show a similar analysis in terms of true wind direction. Here we see normal values for the drag coefficient for northerly wind directions and a broad sector of greatly reduced values for winds from about 120 to 250 deg. The mean values of the bulk variables forcing the fluxes and the stability corrections are also highly correlated with wind direction (Figure 6). Clearly, the most stratified conditions are associated with offshore flow (westerly quadrant) and/or flow from warm to cold water (southerly to southeasterly flow). The correlation of mean wind speed with true wind direction is not as clear-cut, possibly because of the mixing of conditions from different distances from shore. From Fig. 6 we can see that normal values of drag coefficients for northerly flow are associated with stronger surface-layer winds and near-neutral stability. This is because of the initially cooler air for northerly flow and the increasing sea surface temperatures as the flow moves southward. This results in a deep convective boundary layer rather than a shallow stable boundary layer.

The spatial aspects of the phenomenon we have observed can be illuminated by analysis on a geographic grid. Figure 7a shows a contour plot of the drag coefficient ratio in the coastal region. The depressed regions are principally located close to the coast with some correspondence to the largest air-sea temperature differences (Figure 7b), consistent with warm air advection from hot daytime or warm nighttime land boundary-layers. There is some lack of correspondence in the upper Gulf of Maine area near Nova Scotia. The results shown in these figures are corrected for surface-layer stability effects. The bulk Richardson number, $Ri_b(z)$, is a useful index of the surface-layer stability. Stability effects reduce the surface fluxes about a factor of 2 when Ri_b is on the order of 0.05 (corresponding to $z/L = 1.0$). While there is some debate about the correct forms of stability correction functions [*Cheng and Brutsaert*, 2005; *Grachev et al.*, 2006; *Steeneveld et al.*, 2006], they are well established in weak to moderately stable conditions ($z/L<2$ or $Ri_b < 0.08$). Contours of Ri_b (Figure 7c) indicate that strong stability effects are confined much closer to the coast (yellow to reddish contours) than the observable depressions in drag coefficient. Thus, we conclude that reduced neutral drag coefficients observed in NEAQS-04 are not caused by errors in the corrections to neutral values.

Wave-age (W_a) effects in coastal regions can occur with offshore flow or with weak flow in the presence of swell. The conventional wisdom is that young waves in offshore flow cause an increase in fluxes (see section 3). Regardless of the wave effects, we can combine standard scaling theory with our measurements of both C_d and C_h to assess the wave aspects. The COARE algorithm is a typical representation where velocity and scalar roughness lengths are separated as follows:

$$z_o = \alpha(W_a)u_*^2 / g + 0.11\nu / u_* = f(u_*, W_a), \tag{12a}$$

$$z_{ot} = f(R_r), \tag{12b}$$

where α is a wave property-dependent Charnock parameter and $R_r = z_o u_* / \nu$ is the roughness Reynolds number. For wind speeds less than 8 ms^{-1}, we find R_r<1. In this region we expect z_{ot} to be constant at 10^{-4} m or $C_{T10n}^{1/2} \cong 0.0347$. Thus, if the observed decrease in neutral transfer coefficients were due to an ocean wave effect, we expect $C_{d10n}^{1/2}$ to be affected but that $C_{T10n}^{1/2}$ is not affected. However, Figure 8 shows both velocity and temperature coefficients to be similarly affected. Based on this analysis, we rule out a substantial surface wave/fetch effect.

IBL effects are examined by using Richardson Number threshold estimates of the boundary-layer depth, as described in Sec. 5. In stable boundary-layers we expect a quasilinear profile of the fluxes [*Nieuwstadt*, 1985] with a maximum at the surface and near-zero at h.

$$\overline{w'x'}(z) \cong \overline{w'x'}_o(1 - z/h). \tag{13}$$

If the height of the measurement is much smaller than h, then the measurement is equivalent to the surface flux. For the NEAQS-04 case, the flux instruments are at 18 m above the sea surface. Using diagnoses of the depth of the boundary-layer described in Sec. 5, we have composited values for the ratio of the measured to bulk model momentum transfer coefficient in bins of IBL depth (Figure 9). A clear relationship is shown using each of the three Ri_b criteria (0.1, 0.25, or 0.5), but the fit to (13) is better and the scatter is less using the $Ri_b = 0.10$ criterion. The significance of this is not clear. *Nieuwstadt's* [1985] analysis showed that the flux profile for buoyancy was linear, but that the rate of decrease with height of momentum flux was greatest at the surface (i.e., slightly nonlinear). Furthermore, we do not know that the bulk flux calculated from meteorological variables measured at 18 m is a proper surrogate for the true surface flux.

One remarkable feature [*Garratt*, 1992] of the quasi-equilibrium stable boundary-layer is that the buoyancy flux approaches an upper limit independent of the temperature profile. A larger air-sea temperature difference favors a higher heat/buoyancy flux, but this is balanced by the turbulence suppression caused by the increased stratification. Thus,

$$H_{sv\_equilibrium} = -\frac{\rho c_p \theta_v}{g} R_f |f| V_g^2 / \sqrt{3} \cong 0.42 V_g^2, \tag{14}$$

i.e., about -40 Wm^{-2} at a geostrophic wind of 10 ms^{-1}. If we use the sonde wind speed at 250-m height as an estimate of geostrophic wind, then we obtain high correlation with near-surface fluxes (the correlation of V_g^2 with H_{svc} is $r^2 = 0.70$ and with H_{svb} $r^2 = 0.75$) under stable conditions. However, the slope is about ¼ of that given in (14) or, correspondingly, the geostrophic wind speed estimate we are using is about a factor of 2 too large. The reduced heat flux (relative to [14]) may imply that the 250-m wind speed is overshooting the geostrophic wind (the low-level jet), or the suppression effects of the stratification in the IBL are dominating in the near field. Another possibility is that a significant additional heat transfer could be by IR radiative flux (*Steeneveld et al.*, 2006).

7. Ozone Deposition

Direct measurements of ozone fluxes were not made on the cruise. However, we have computed estimates of ozone deposition velocity, V_{doz} , using the ozone version of the NOAA COARE gas transfer model. The basics of the gas transfer model are described in *Fairall et al.* [2000] and *Hare et al.* [2004]. The specifics for the ozone version are described in *Fairall et al*. [2006] but are summarized here. The flux of ozone to the ocean, F_x, is represented as

$$F_x = -V_{doz} X_{oz}, \tag{15}$$

where X_{oz} is the atmospheric ozone concentration at reference height.

The deposition velocity in the NOAA COARE parameterization is

$$V_{doz} = [R_a + (\alpha V_w)^{-1}]^{-1}, \tag{16}$$

where R_a is the atmospheric transfer resistance (sm^{-1}), V_w is the oceanic transfer velocity associated with the destruction of ozone by chemical reaction in the water, and α is the solubility of ozone in seawater. The oceanic transfer velocity is given by

$$V_w = \sqrt{aD_x}\,\frac{K_1(\xi_0)}{K_0(\xi_0)}, \tag{17}$$

$$\xi_0 = \frac{2}{ku_*}\sqrt{aD_x}, \tag{18}$$

where $a \approx 10^3$ s^{-1} is the chemical reactivity of ozone in the water, D_x the molecular diffusivity of ozone in seawater, and K_o and K_1 are modified Bessel functions.

Observed deposition velocities are reported in the literature with values ranging from $V_{doz} \sim 0.1$ to 1.2 mm s^{-1} for ocean water [*Ganzeveld et al*., 2005]. We have used Equations (16) and (17) to compute deposition velocities for the NEAQS-04 time series and find similar values. Contour plots of the spatial distribution of the computed deposition velocities are shown in Figures 10a and 10b. The first figure uses the bulk algorithm for u_*, while the second uses the direct measurements of u_*. Both maps show the same basic features with highest values just northeast of Cape Cod and the lowest values close to the coast.

8. Conclusions

The NEAQS/ICARTT field program in the summer of 2004 was a unique ship-based study of surface fluxes and stable boundary-layers in the coastal regions. The extensive suite of measurements offer an unprecedented – perhaps even perplexing – view of IBL and surface flux processes in this regime. The analysis presented here, though preliminary, clearly indicates that tried-and-true open-ocean bulk flux relationships become inaccurate close to shore. We found significantly lower fluxes (as determined by direct measurement) than expected; the reduction corresponding to light winds, winds from the south-southeast sector, proximity to shore, and/or very shallow boundary-layer depths. All of these factors are correlated, so it is a complicated problem.

It appears that reduced fluxes are not caused by a measurement problem, a MOST stability correction problem, or wave-age effects.

Our analysis suggests that the depth of the stable boundary-layer is a critical parameter associated with reduced surface fluxes. The low fluxes observed at lighter wind speed and/or westerly winds result from their joint occurrence with shallow boundary layers. One interpretation is that the bulk algorithm is giving approximately the correct surface flux, but our instruments do not realize the full value because of the flux profile (the flux approaches zero at the IBL depth). Thus, the flux reduction is greater for shallow BLs. *Mahrt et al.* [1998] found a similar reduction for sensible heat but not for stress. However, their measurements were closer to the coast (2–4 km fetch) where wave-age effects may be more significant. One interesting aspect of this problem is diagnosing the depth of the BL without profiles of the turbulent fluxes. We have examined gradient Richardson number, bulk Richardson number, and velocity variance profiles. Analysis of the ratio of the direct flux to the bulk flux suggests that the BL height determined as $R_{ib}(h)$=0.10 gives the most consistent estimates. This is often (but not always) consistent with the 0.25 gradient Richardson number criterion. A peak in the lidar-derived velocity variance, when present, was often much higher, suggesting that gravity waves are dominating that signal. Based on the 0.10 criterion, the typical BL depth was less than 50 m, and only a few percent exceeded 200 m for the locations of the sonde launches.

Besides BL depth, we examined other basic properties of the flow. In an effort to classify the gross stability of the BL for each sounding, we computed the bulk Richardson number at 250 m height. Only 10% were less than 0.25, 10% exceeded 5, and the median was 0.5. *Garratt* [1992] predicted that buoyancy flux would prove to be independent of the thermodynamic lid on the BL and would scale as the square of the geostrophic wind speed. We found the surface buoyancy flux to be highly correlated with the wind speed at 250 m (which we took as a surrogate for the geostrophic wind), but the values were about ¼ of *Garratt's* [1992] prediction. This is consistent with the BL depth being a better fit with $R_{ib}(h)$=0.10 instead of a value between 0.25 and 0.50. The wind profiles were strongly sheared with the flow being often westerly at 250 m, while the near-surface flow was southerly. The combination of the strong diurnal cycle over land and the baroclinic flow regime further confuses efforts to understand this system. *Zilitinkevic and Esau* [2003] examined observations and LES studies and found baroclinicity increased the equilibrium depth of stable boundary layers, but their formula gives much lower boundary layer depths than we observed. We speculate that baroclinicity associated with sloping boundary layers tends to concentrate velocity shear at 90 degrees to the local mean wind direction near the top of the IBL and that this leads to a lower IBL depth either because this configuration generates turbulence less efficiently or it is more efficiently dissipated locally (before it can drive mixing). We did not examine diurnal effects but some discussion can be found in *Angevine et al.* [2006]

One amusing twist on the complexity was our estimates of ozone deposition velocity in the Gulf of Maine region. Values were distributed between 0 and 1 mms^{-1} with a median of 0.44 mm s^{-1}; this value yields an e-folding time for surface removal of ozone from the boundary-layer of about 1 day. The different indirect versus bulk friction velocity values made little difference in the spatial distribution because the reactivity level we chose made deposition velocity less sensitive to wind forcing. Note that we estimated deposition velocity and not the actual loss of ozone to the surface (i.e., the product of deposition velocity and concentration).

NEAQS-04 was principally a pollution experiment and was not designed to uncover unifying principles in coastal IBL physics, but a wealth of data remains unexplored. We anticipate that further investigation of the relationship between the gross stability, distance from shore, and BL depth might shed more light on the problem, although the challenge is to keep the number of variables significantly less than the number of data points.

Acknowledgements. The authors thank all of the participants in ICARTT/NEAQS 2004 who aided in the operation of these instruments and the collection of data. A special thanks goes to the dedicated officers and crew of the NOAA R/V *Ronald H. Brown*. This work was supported by the NOAA Health of the Atmosphere program, the NOAA Carbon Cycle program, and the NOAA ESRL Physical Sciences Division Director's Fund.

References

Angevine, W. M., J. E. Hare, C. W. Fairall, D. E. Wolfe, R. J. Hill, W. A. Brewer, and A. B. White (2006), Structure and formation of the highly stable marine boundary-layer over the Gulf of Maine *J. Geophys. Res*., to appear (this issue).

Cheng, Y., and W. Brutsaert (2005), Flux-profile relationships for wind speed and temperature in the stable atmospheric boundary-layer, *Bound-Layer Meteorol*., *114*(3), 519–538.

Donelan, M. A. (1982), The dependence of the aerodynamic drag coefficient on wave parameters, in *First International Conference on Meteorology and Air-Sea Interaction of the Coastal Zone*, pp. 381–387, American Meteorological Society, Boston, Mass.

Donelan, M. A., F. W. Dobson, S. D. Smith and R. J. Anderson (1982), On the dependence of sea surface roughness on wave development, *J. Phys. Oceanogr.* *23*, 2143–2149.

Edson, J. B., and C. W. Fairall (1998), Similarity relationships in the marine atmospheric surface layer for terms in the TKE and scalar variance budgets. *J. Atmos. Sci.*, *55*, 2311–2338.

Edson, J. B., A. A. Hinton, K. E. Prada, J. E. Hare, and C. W. Fairall (1998), Direct covariance flux estimates from moving platforms at sea. *J. Atmos. Oceanic Tech.*, *15*, 547–562.

Fairall, C. W., and G. S. Young (1991), A field evaluation of shipboard performance of an infrared hygrometer, *Proceedings of the 7th AMS Symposium on Meteorological Observations and Measurements*, pp. 311–315, New Orleans.

Fairall, C. W., E. F. Bradley, D. P. Rogers, J. B. Edson, and G. S. Young (1996a), Bulk parameterization of air–sea fluxes in TOGA COARE, *J. Geophys. Res.*, *101*(C2), 3747–3767.

Fairall, C. W., E. F. Bradley, J. S. Godfrey, G.A. Wick, J. B. Edson, and G. S. Young (1996b), Cool skin and warm layer effects on the sea surface temperature, *J. Geophys. Res., 101*, 1295–1308.

Fairall, C. W., A. B. White, J. B. Edson, and J. E. Hare (1997), Integrated shipboard measurements of the marine boundary-layer, *J. Atmos. Oceanic Technol., 14*, 338–359.

Fairall, C. W., J. E. Hare, J. B. Edson and W. McGillis (2000), Parameterization and measurement of air-sea gas transfer. *Bound.-Layer Meteorol.*, *96*, 63–105.

Fairall, C. W., E. F. Bradley, J. E. Hare, A. A. Grachev, and J. B. Edson (2003), Bulk parameterization of air-sea fluxes: Updates and verification for the COARE algorithm, *J. Clim.*, *16*(4), 571 – 591.

Fairall, C. W., J. E. Hare, D. Helmig, and L. Ganzveld, 2006: Water-side turbulence enhancement of ozone deposition to the ocean. *Atm. Chem. Phys. Disc*, SRef-ID: 1680-7375/acpd/2006-6-5137, 5137-5162.

Fehsenfeld, F.C., *et al.* (2006), International Consortium for Atmospheric Research on Transport and Transformation (ICARTT): North America to Europe: Overview of the 2004 summer field study, *J. Geophys. Res.*, submitted (this issue).

Finkelstein, P. L., and P. F. Sims (2001), Sampling error in eddy correlation flux measurements, *J. Geophys. Res.*, *106*, 3503–3509.

Friehe, C., W. J. Shaw, D. P. Rogers, K. L. Davidson, W. G. Large, S. A. Stage, G. H. Crescenti, S. J. S. Khalsa, G. K. Greenhut, and F. Li (1991), Air-sea fluxes and surface layer turbulence around a sea surface temperature front, *J. Geophys. Res.*, *96C*, 8593–8609.

Ganzeveld L., D. Helmig, J. Hare and C. Fairall (2005), Ozone deposition to oceans and lakes and its role in the tropospheric ozone budget, *Global Biogechem. Cycles.* To appear.

Garratt, J. R. (1987), The stably stratified internal boundary-layer for steady and diurnally varying offshore flow, *Boundary-layer Meteorol*. *38*(4), 369–394.

Garratt, J. R. (1990), The internal boundary-layer - A review, *Boundary-layer Meteorol*., *50*, 171–203.

Garratt, J. R. (1992), *The Atmospheric Boundary-layer*, 316 pp., Cambridge University Press, Cambridge, UK.

Garratt, J. R.and B. F. Ryan (1989), The structure of the stably stratified internal boundary-layer in offshore flow over the sea, *Boundary-layer Meteorol*., *47*, 17–40.

Geernaert, G. L., S. E. Larsen, and F. Hansen (1987), Measurements of the wind stress, heat flux and turbulence intensity during storm conditions over the North Sea, *J. Geophys. Res., 92*, 127–139.

Godfrey, J. S., and A. C. M. Beljaars (1991), On the turbulent fluxes of buoyancy, heat, and moisture at the air–sea interface at low wind speeds, *J. Geophys. Res*., *96*, 22,043–22,048.

Grachev, A. A., and C. W. Fairall (2001), Upward Momentum transfer in the marine boundary-layer, *J. Phys. Oceanogr.*, *31*(7), 1698–1711.

Grachev, A. A., E. L Andreas, C. W. Fairall, P. S. Guest, and P. O. G. Persson (2006), SHEBA flux-profile relationships in the stable atmospheric surface layer, *Boundary-layer Meteorol.*, submitted.

Hare, J. E., C. W. Fairall, W. R. McGillis, B. Ward, and R. Wanninkhof (2004) Evaluation of the NOAA/COARE air-sea gas transfer parameterization using GasEx data, *J. Geophys. Res*., 109 Art. No. C08S11, doi:10.1029/2003JC001831.

Kitaigorodskii, S. A. (1998), *The Physics of Air-Sea Interaction*, translated from Russian, 273 pp., Israel Program for Scientific Translations, Jerusalem,1970.

Mahrt, L., D. Vickers, J. Edson, J. Sun, J. Hojstrup, J. Hare and J. Wilczak, Heat flux in the coastal zone, *Boundary-layer Meteorol.*, *86*(3), 421–4461998.

Mahrt, L. (1999), The Coastal Zone. In *Air-Sea Exchange: Physics, Chemistry and Dynamics*, Edited by G. Geernaert, 246–267, Kluwer.

Mahrt, L., D. Vickers, J. Sun, T. Crawford, G. Crescenti, and P. Frederickson (2001), Surface stress in offshore flow and quasi-frictional decoupling, *J. Geophys. Res.*, *106*(D18), 20,629–20,639.

Nieuwstadt, F. T. M. (1984), The Turbulent Structure of the Stable, Nocturnal Boundary Layer, *J. Atmos. Sci. 41*, 2202 – 2216.

Rieder, K. F. (1997), Analysis of sea surface drag parameterizations in open ocean conditions, *Boundary-layer Meteorol.*, *82*(3), 355–377.

Rogers, D. P., D. W. Johnson, and C. A. Friehe (1995), The stable internal boundary-layer over a coastal sea. Part I: Airborne measurements of the mean and turbulence structure, *J. Atmos. Sci.*, *52(6)*, 667–683.

Rotunno, R. A. (1992), Synopsis of Coastal Meteorology: A Review of the State of the Science, in *Environmental Science in the Coastal Zone: Issues for Further Research*, (Proceedings of a retreat held at the J. Erik Jonsson Woods Hole Center Woods Hole, Massachusetts June 25–26), 184 pp, National Academy Press Washington, D.C..

Skyllingstad, E. D., R. M. Samelson, L. Mahrt, and P. Barbour (2005), A numerical modeling study of warm offshore flow over cool water, *Mon. Weather Rev.*, *133*, 345–361.

Smedman, A.-S., H. Bergstroem, and B. Grisogono (1997), Evolution of stable internal boundary-layers over a cold sea, *J. Geophys. Res.*, *102*, 1091–1099.

Smith, S. D., R. J. Anderson, W. A. Oost, C. Kraan, N. Maat, J. DeCosmo, K. B. Katsaros, K. L. Davidson, K. Bumke, L. Hasse, and H. M. Chadwick (1992), Sea surface wind stress and drag coefficients: The HEXOS results, *Boundary-layer Meteorol.*, *60*, 109–142.

Snyder, R. L., F. W. Dobson, J. A. Elliott, and R. B. Long (1981), Array measurements of atmospheric pressure fluctuations above surface gravity waves, *J. Fluid Mech.* *102*, 1–59.

Steeneveld, G. J., B. J. H. van de Wiel, and A. A. M. Holtslag (2006), Modeling the evolution of the atmospheric boundary-layer coupled to the land surface for three contrasting nights in CASES-99, *J. Atmos. Sci*., *63*, 920–935.

Sullivan, P.P., J.B. Edson, J.C. McWilliams, C-H. Moeng (2004), Large-Eddy Simulations and observations of wave driven boundary layers, *16th Symposium on Boundary Layer and Turbulence*, American Meteorology Society, Portland, ME.

Sullivan, P. P., J. B. Edson, T. Hristov, and J. C. McWilliams (2006), Momentum flux structures and statistics in low-wind marine surface layers: Observations and large-eddy simulations, *27th Conference on Hurricanes and Tropical Meteorolog*y, American Meteorology Society, Monterey, CA.

Sun, J., D. Vandemark, L. Mahrt, D. Vicker, T. Crawford, C. Vogel (2001), Momentum transfer over the coastal zone, *J. Geophys. Res.*, *106*(D12), 12,437–12,448.

Tanner, C. B. and G. W. Thurtell (1969), Anemoclinometer measurements of Reynolds stress and heat transport in then atmospheric surface layer, *University of Wisconsin Technical Report ECOM-66-G22-F*, 82 pp. [Available from U.S. Army Electronic Command, Atmospheric Sciences Laboratory, Ft. Huachuca, AZ 85613.]

Vickers, D. and L. Mahrt, Fetch limited drag coefficients, *Boundary-layer Meteorol*. (1997), *85*, 53–79.

Vickers, D. and L. Mahrt, Observations of nondimensional shear in the coastal zone (1999), *Q. J. R. Meteorol. Soc.*, *125*(559A), 2685–2702.

Vickers, D., L. Mahrt, J. Sun, and T. Crawford, Structure of offshore flow (2001), *Mon. Weather Rev.*, *129*, 1251–1258.

Wolfe, D. E., C.W. Fairall, D.C. Welsh, M. Ratterree, A.W. Brewer, J.M. Intrieri, C.J. Senff, B.J. McCarty, S. Tucker, D.C. Law, A.B. White, and D.E. White (2006), Shipboard multi-sensor merged wind profilers from NEAQS-04: Radar wind profiler, high-resolution Doppler lidar, GPS rawinsonde, *J. Geophys. Res.*, to appear (this issue).

Zilitinkevich, S. S., and I. N. Esau (2003), The effect of baroclinicity on the equilibrium depth of neutral and stable planetary boundary layers. *Q. J. R. Meteorol. Soc., 129*, 3339-3356.

Figure Captions

Figure 1. The positions of 4 rawinsonde launches relative to the coast are indicated by the red symbols, and the time (UTC) as yy mm dd hh mm is in the title. Wind vectors at 17.5 m (red) and 250 m (black) at the launch positions are shown; one degree of longitude corresponds to 3 m/s.

Figure 2a. Data corresponds to case (a) in Figure 1: Rawinsonde data: blue diamonds; lidar data: green pluses; lidar data interpolated to sonde-data heights: green Xs; ship-board sonic anemometer, thermometer, hygrometer data: red asterisk; Gradient Richardson numbers using lidar velocity in place of sonde velocity: green pluses. Vertical dashed lines indicate Richardson numbers of 0.1, 0.25, and 0.5

Figure 2b. Data correspond to case (b) in Figure 1: See Figure 2a caption.

Figure 2c. Data correspond to case (c) in Figure 1. See Figure 2a caption.

Figure 2d. Data correspond to case (d) in Figure 1. See Figure 2a caption.

Figure 3. Turbulent transfer coefficients as a function of 10-m neutral wind speed. The blue diamonds are individual 1-hr averages. The solid red line is the COARE algorithm. The circles (with 1-sigma median limits) are the medians within wind-speed bins as

described by Equation (11). Upper panel (a) is the momentum coefficient; lower panel (b) is the sensible heat coefficient.

Figure 4a. Turbulent cospectra as a function of frequency $\overline{w'u'}$ (upper panel), $\overline{w'T'}$ (middle panel), and $\overline{w'q'}$ (lower panel). The cospectral values are multiplied by frequency so the graph is area-preserving. Four hours of data are shown (day 198 0000 to 0300 UTC; wind speed 7.4-8.0 ms^{-1}) with a line for each hour.

Figure 4b. As in Fig. 4a, but for day 214 0100 to 0300 UTC; wind speed 5.4-7.5 ms^{-1}.

Figure 5. Turbulent momentum transfer coefficient as a function of true wind direction: The solid red line is the COARE algorithm. The circles are the medians within wind-direction bins as described by Equation (11); vertical bars are 1-sigma median limits.

Figure 6. Bulk meteorological variables as a function of true wind direction: the upper panel is the number of 1-hr observations, the lower panel shows the medians within wind-direction bins for wind speed (solid line), air-sea humidity difference (circles), and air-sea potential temperature difference (dashed line).

Figure 7a. Contour plot of the ratio of measured 10-m neutral momentum transfer coefficient to values for the open ocean (COARE3.0). Cape Cod is the feature in the lower left corner and Nova Scotia is in the upper right corner.

Figure 7b. As in Figure 7a but for the sea-air temperature difference.

Figure 7c. As in Fig. 7a but for $\log Ri_b$ at the measurement height (17.5 m).

Figure 8. Turbulent 10-m neutral transfer coefficient variables averaged in wind speed bins (momentum flux: circle – measured, solid line – COARE3.0; sensible heat: diamond – measured, dashed line – COARE3.0). The upper panel shows the transfer coefficients computed using Equation (11) as in Fig. 3, the lower panel shows the corresponding values of $c_{x10n}^{1/2}$ computed using Equation (5).

Figure 9. The ratio of measured 10-m neutral momentum transfer coefficient to values for the open ocean (COARE3.0) as a function of boundary-layer depth: circles are the individual 1-hr values, x's are medians, diamonds are means, and the thick dashed line is using Equation (13). Different panels are for different $R_{ib}(z)$ threshold values to define H: (a) Ri_b = 0.10, (b) Ri_b = 0.25, and (c) Ri_b = 0.50.

Figure 10. Contour plot of the Ozone deposition velocity using the model of *Fairall et al.* [2006]: upper panel, u_* from COARE3.0 and lower panel, u_* from direct measurement.

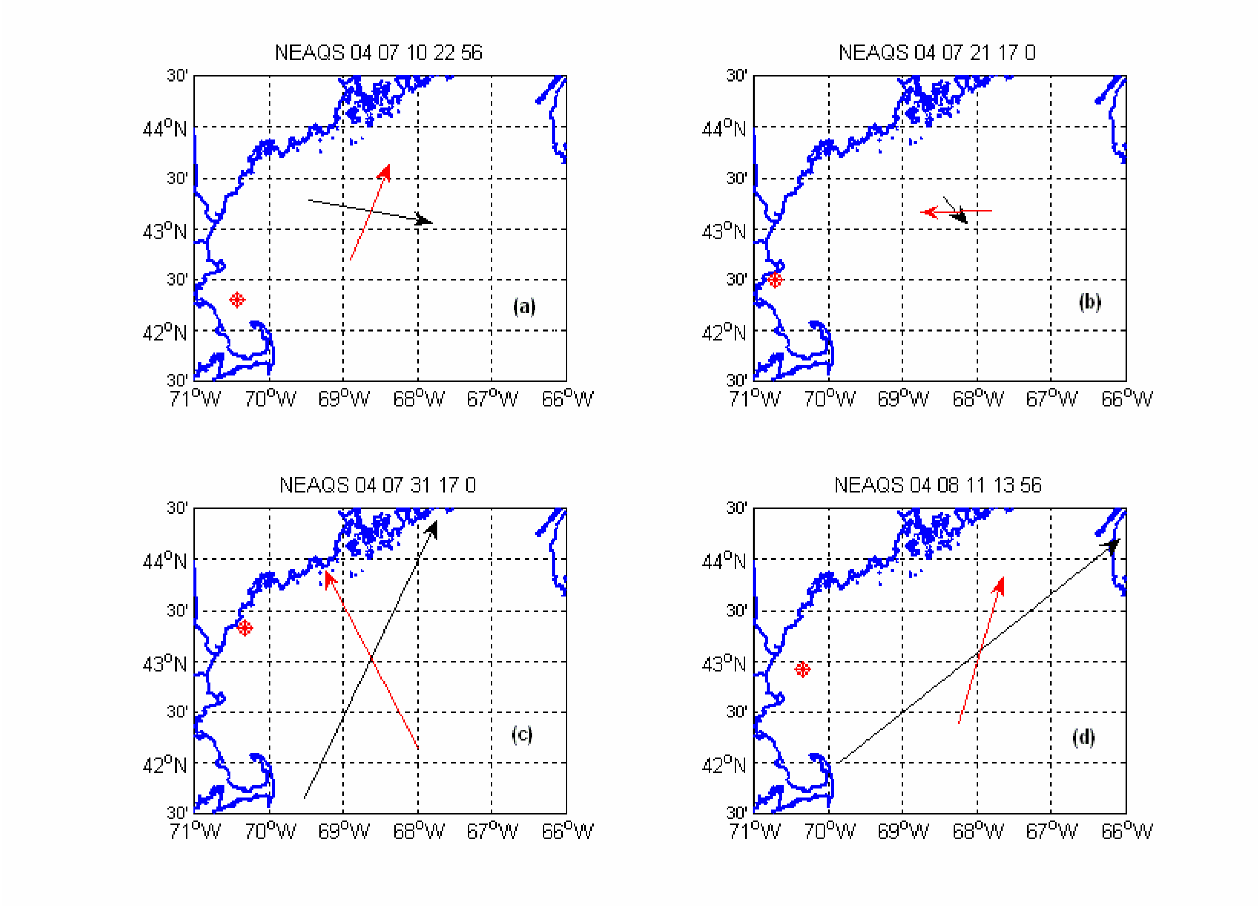

Figure 1. The positions of 4 rawinsonde launches relative to the coast are indicated by the red symbols, and the time (UTC) as yy mm dd hh mm is in the title. Wind vectors at 17.5 m (red) and 250 m (black) at the launch positions are shown; one degree of longitude corresponds to 3 m/s. Cape Cod is the feature in the lower left corner and Nova Scotia is in the upper right corner.

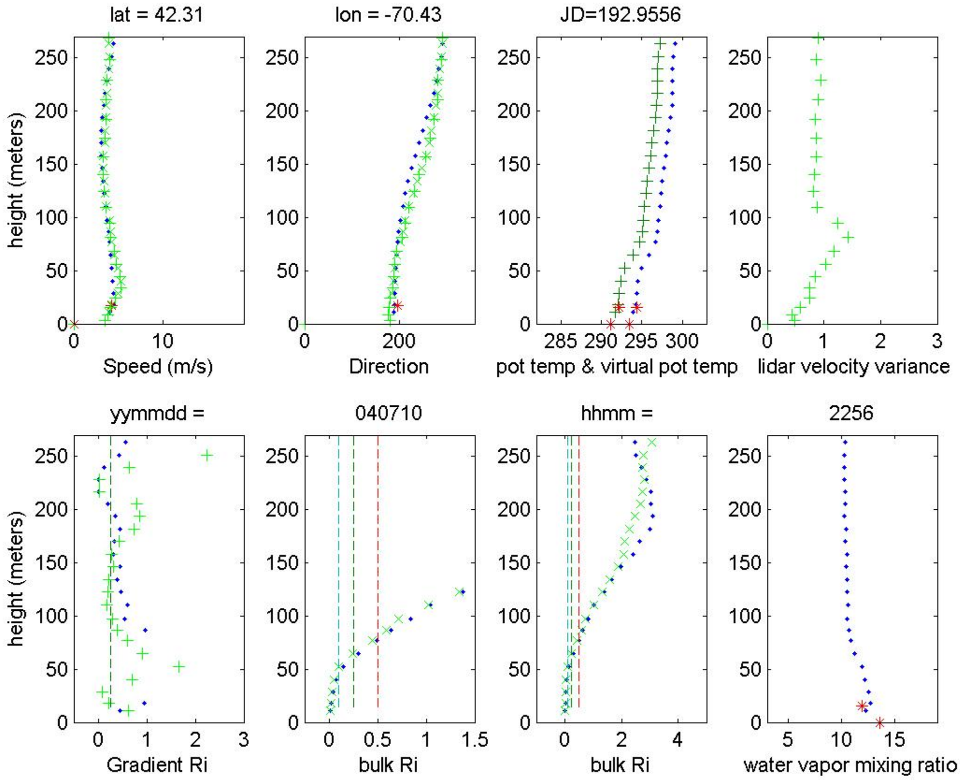

Figure 2a. Data corresponds to case (a) in Figure 1: Rawinsonde data: blue diamonds; lidar data: green pluses; lidar data interpolated to sonde-data heights: green Xs; ship-board sonic anemometer, thermometer, hygrometer data: red asterisk; Gradient Richardson numbers using lidar velocity in place of sonde velocity: green pluses. Vertical dashed lines indicate Richardson numbers of 0.1, 0.25, and 0.5

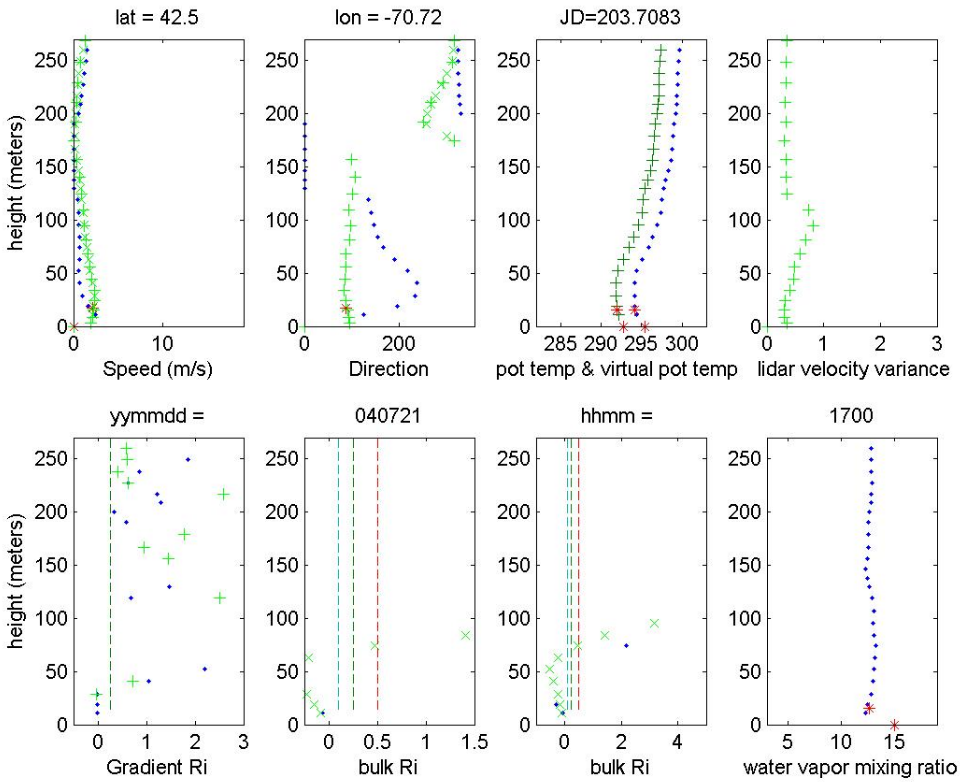

Figure 2b. Data corresponds to case (b) in Figure 1. See Figure 2a caption.

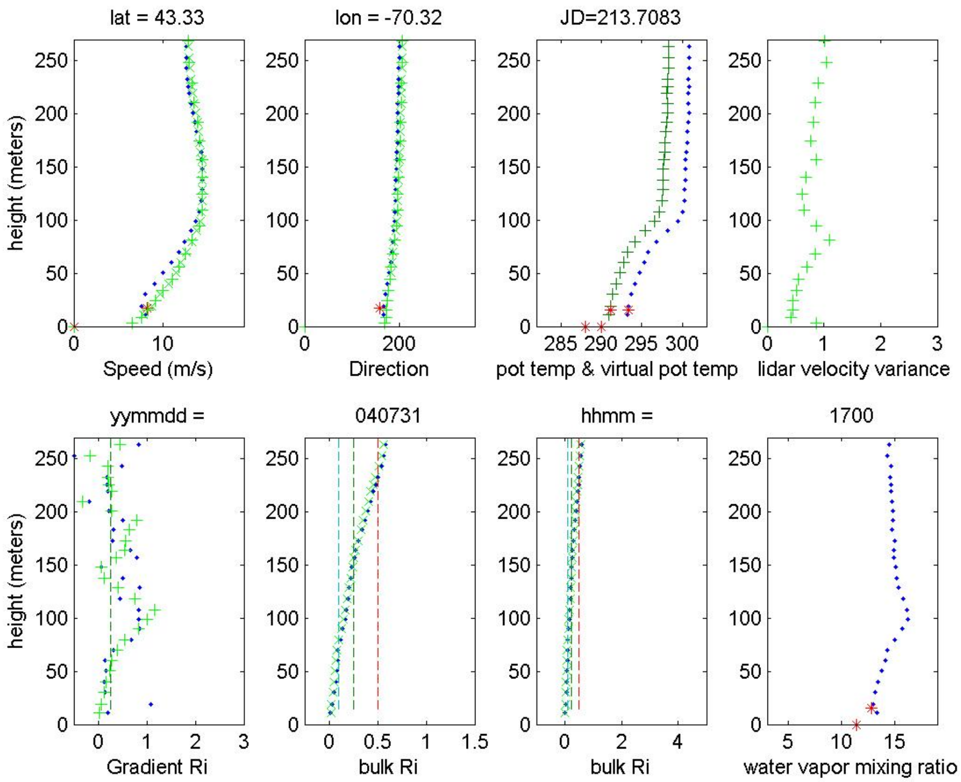

Figure 2c. Data corresponds to case (c) in Figure 1. See Figure 2a caption.

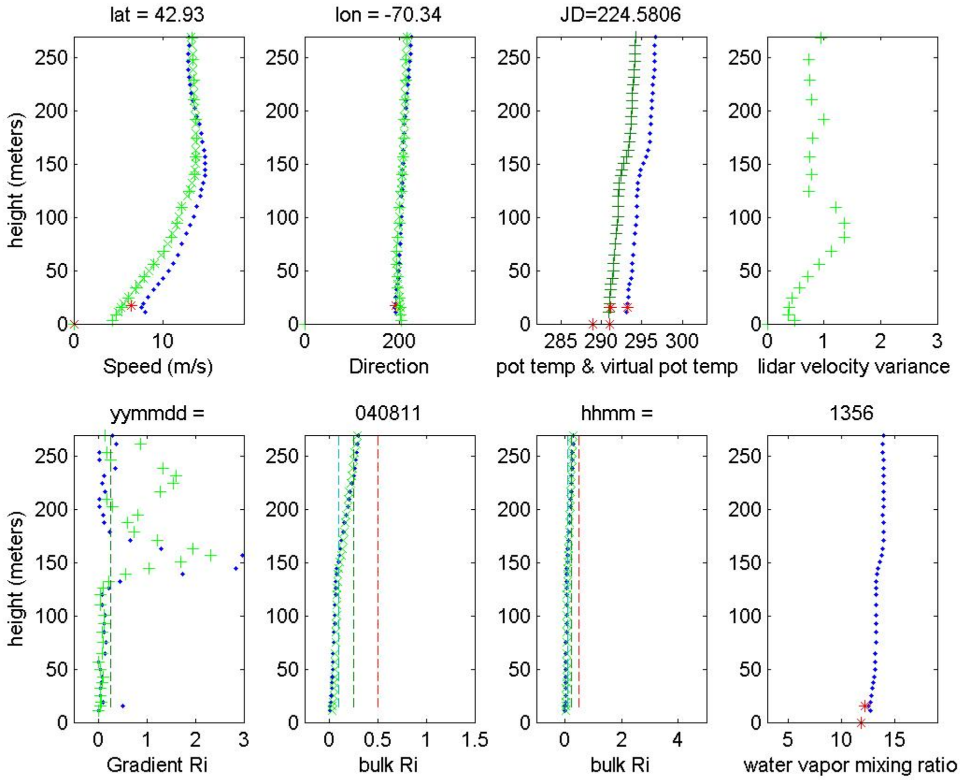

Figure 2d. Data corresponds to case (d) in Figure 1. See Figure 2a caption.

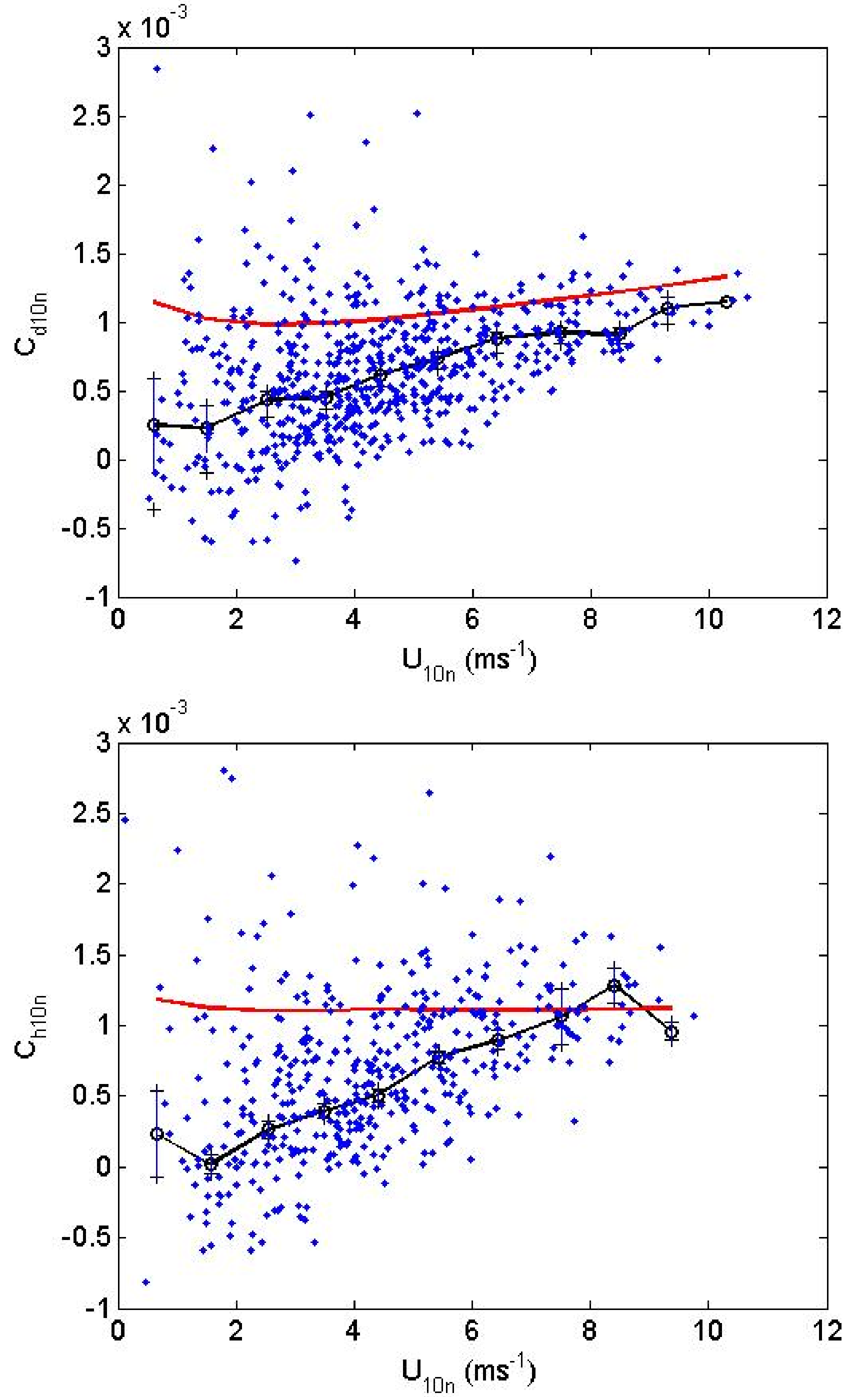

Figure 3. Turbulent transfer coefficients as a function of 10-m neutral wind speed. The blue diamonds are individual 1-hr averages. The solid red line is the COARE algorithm. The circles (with 1-sigma median limits) are the medians within wind-speed bins as described by Equation (11). Upper panel (a) is the momentum coefficient; lower panel (b) is the sensible heat coefficient.

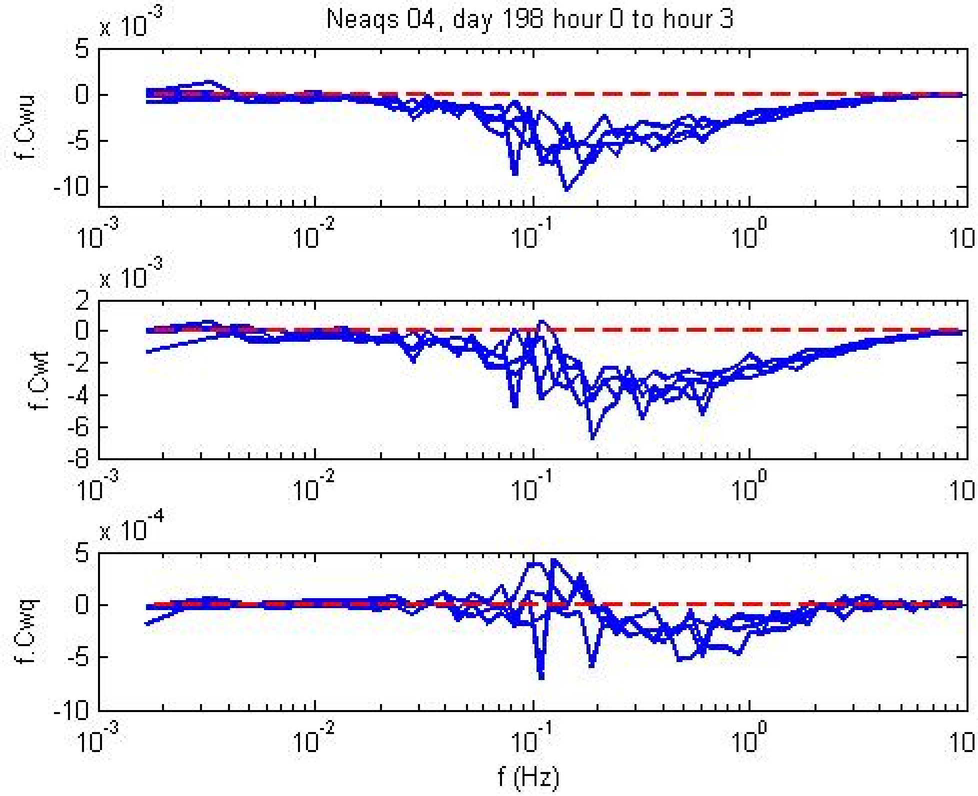

Figure 4a. Turbulent cospectra as a function of frequency $\overline{w'u'}$ (upper panel), $\overline{w'T'}$ (middle panel), and $\overline{w'q'}$ (lower panel). The cospectral values are multiplied by frequency so the graph is area-preserving. Four hours of data are shown (day 198 0000 to 0300 UTC; wind speed 7.4-8.0 ms^{-1}) with a line for each hour.

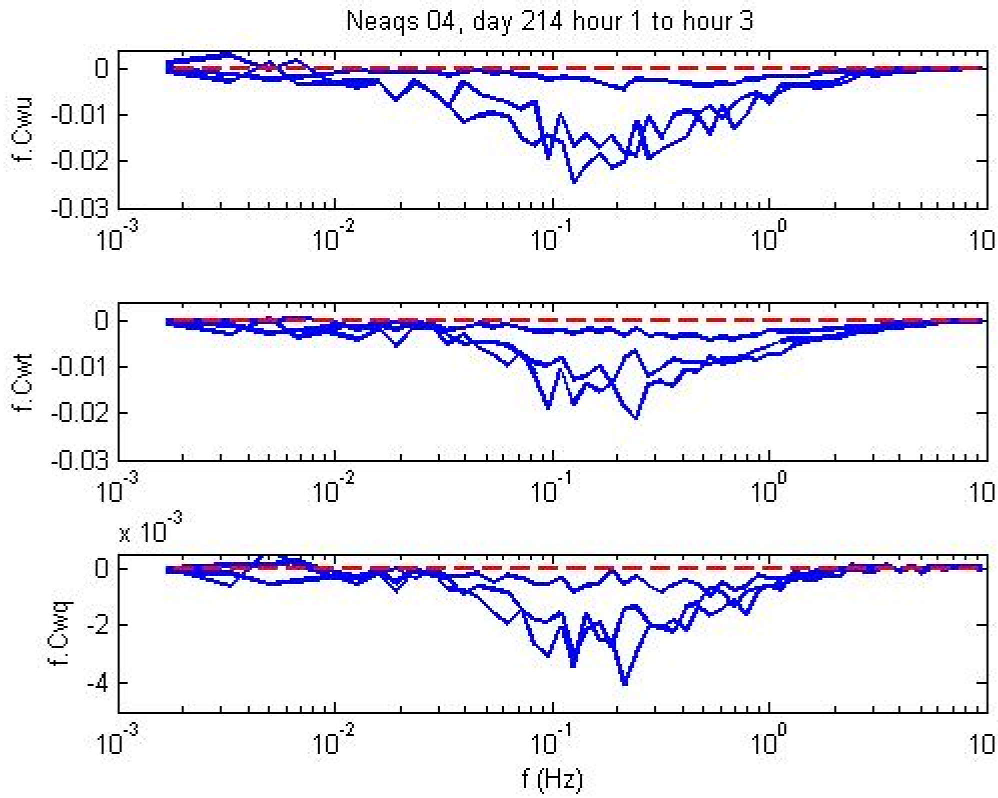

Figure 4b. As in Figure 4a, but for day 214 0100 to 0300 UTC; wind speed 5.4-7.5 ms^{-1}.

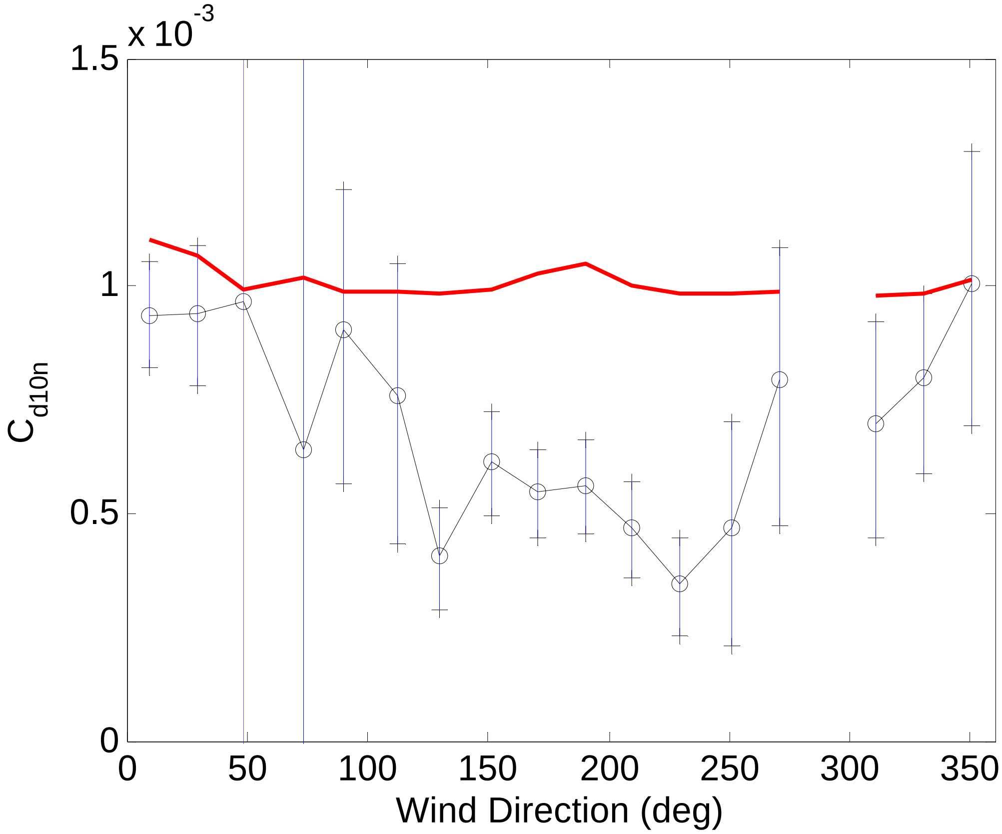

Figure 5. Turbulent momentum transfer coefficient as a function of true wind direction: The solid red line is the COARE algorithm. The circles are the medians within wind-direction bins as described by Equation (11); vertical bars are 1-sigma median limits.

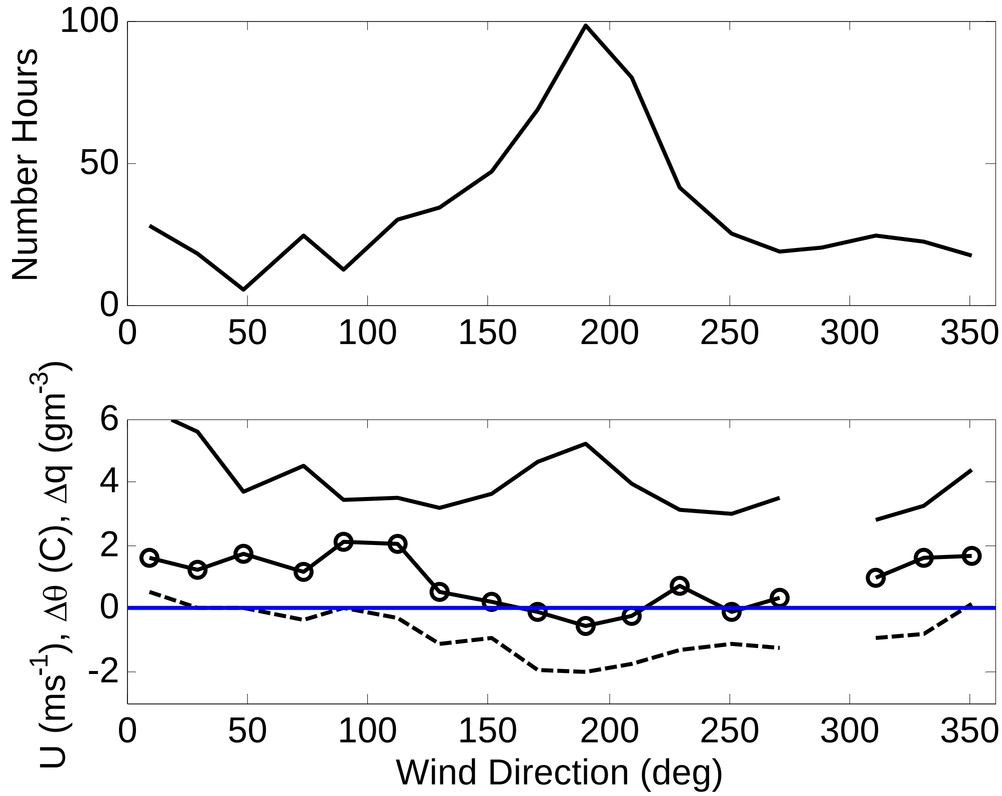

Figure 6. Bulk meteorological variables as a function of true wind direction: the upper panel is the number of 1-hr observations, the lower panel shows the medians within wind-direction bins for wind speed (solid line), air-sea humidity difference (circles), and air-sea potential temperature difference (dashed line).

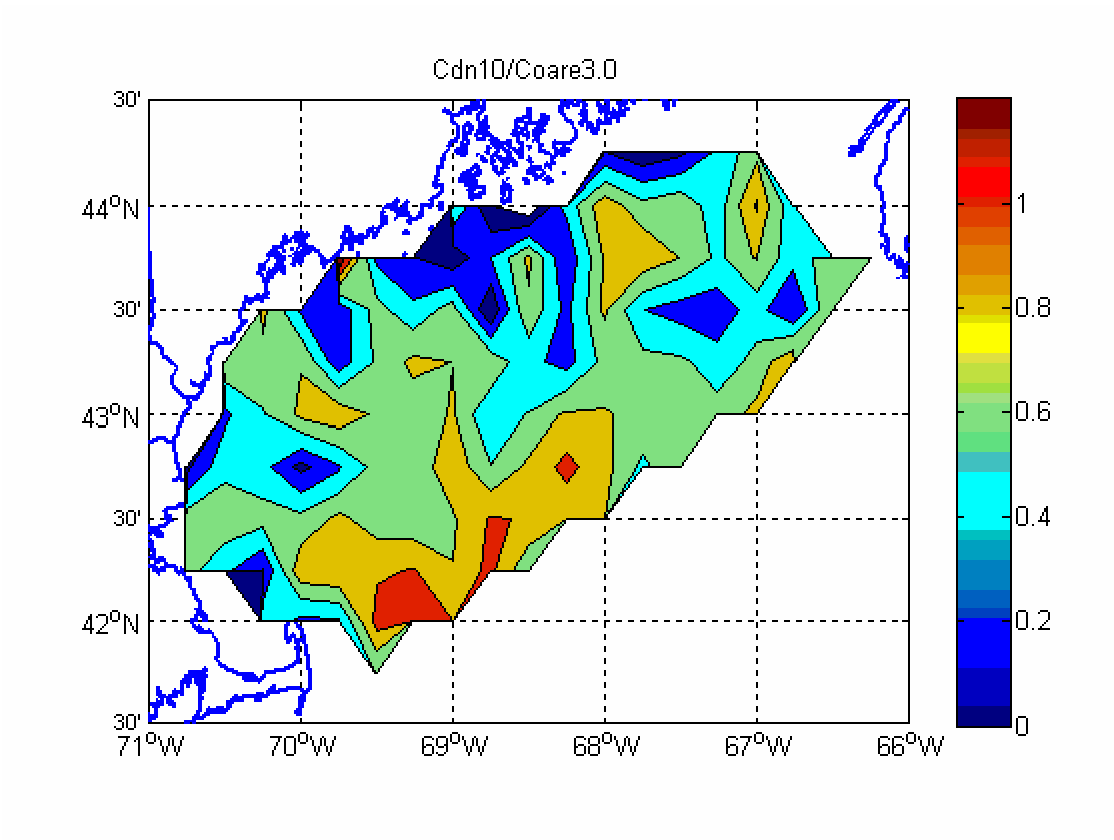

Figure 7a. Contour plot of the ratio of measured 10-m neutral momentum transfer coefficient to values for the open ocean (COARE3.0).

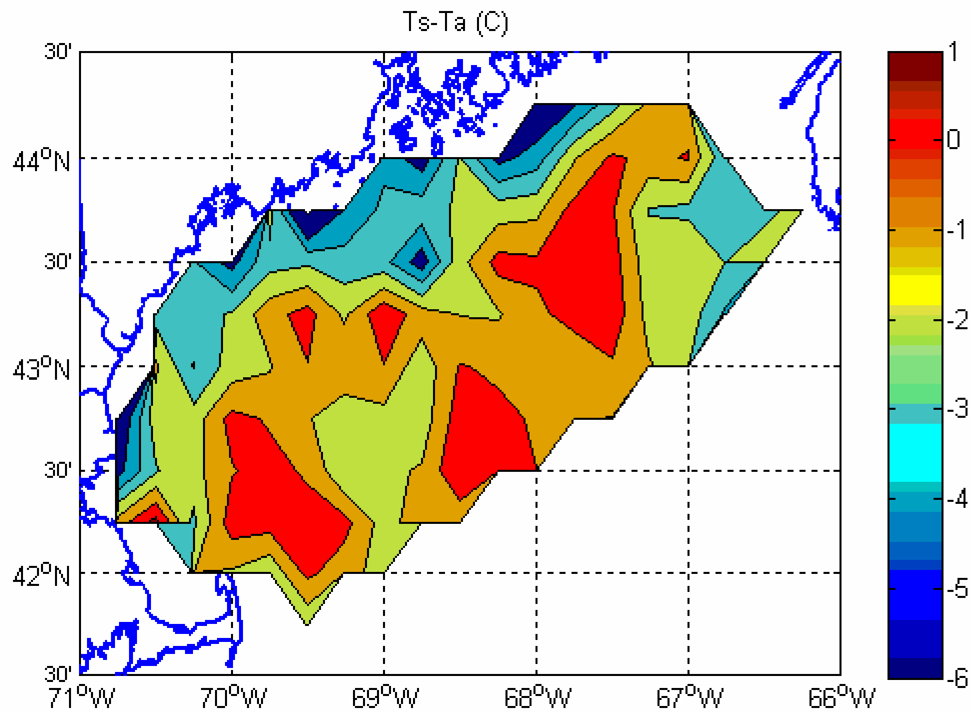

Figure 7b. As in Figure 7a but for the sea-air temperature difference.

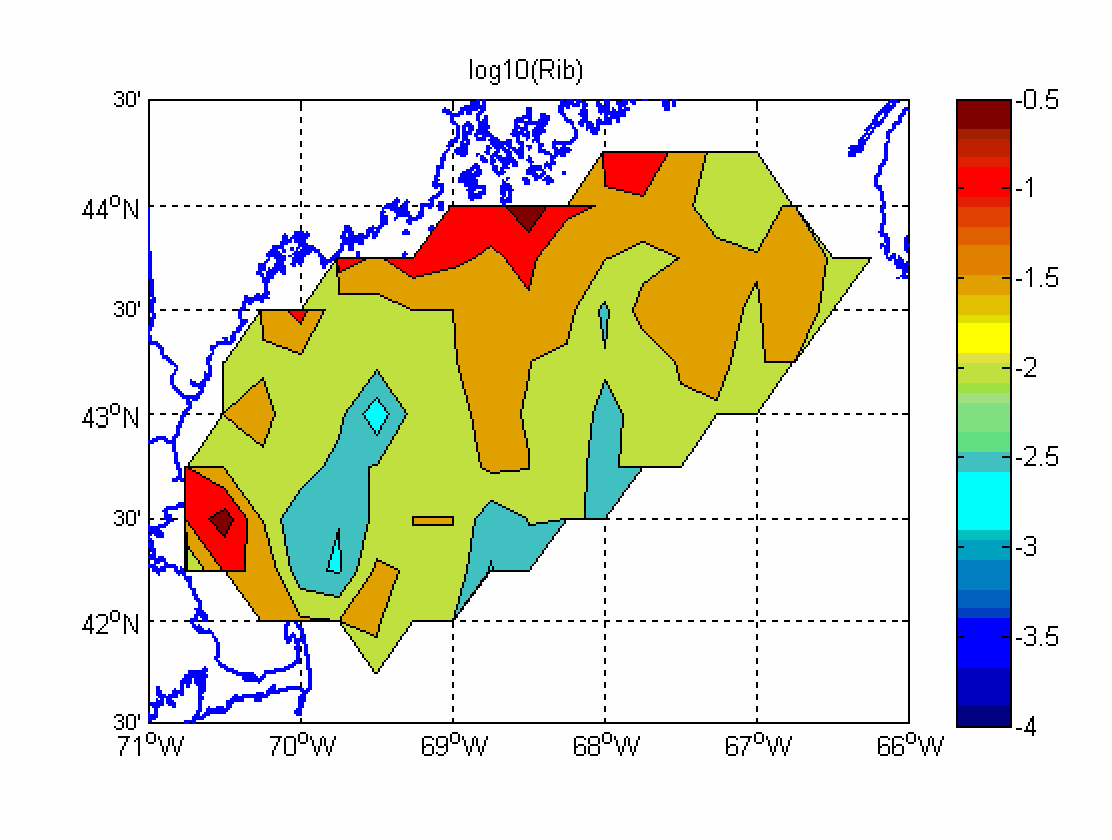

Figure 7c. As in Figure 7a but for $\log Ri_b$ at the measurement height (18-m).

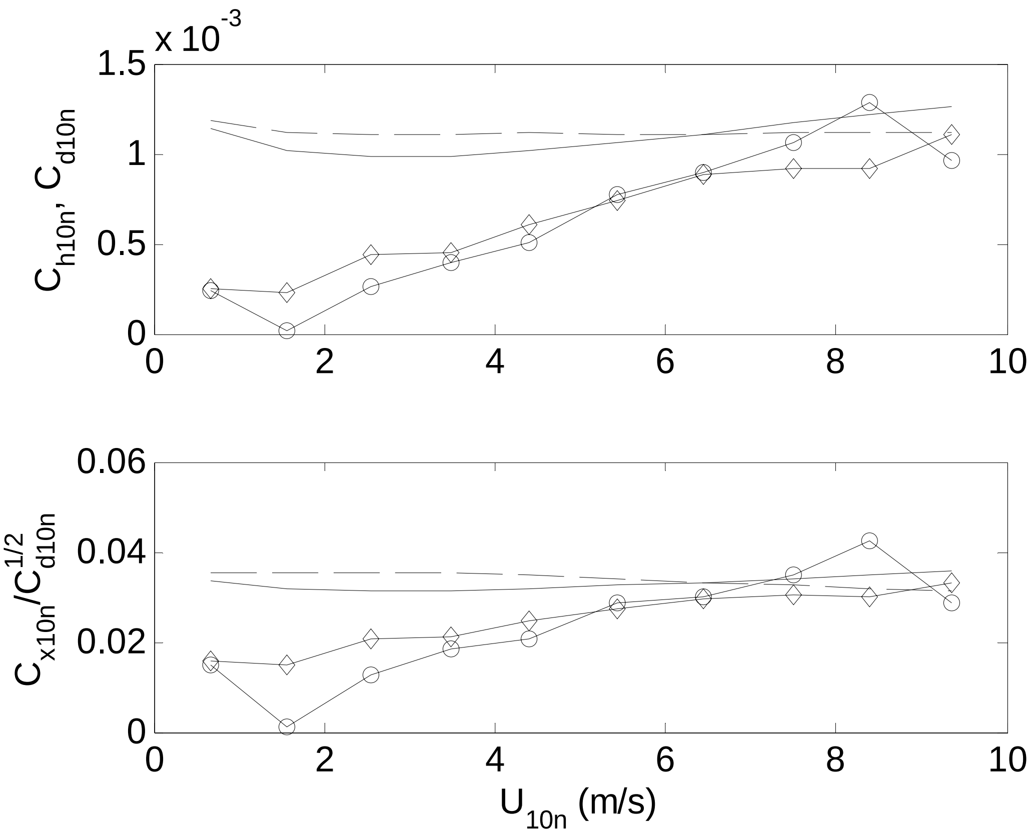

Figure 8. Turbulent 10-m neutral transfer coefficient variables averaged in wind speed bins (momemtum flux: circle – measured, solid line – COARE3.0; sensible heat: diamond – measured, dashed line – COARE3.0). The upper panel shows the transfer coefficients computed using Equation (11) as in Figure 3, the lower panel shows the corresponding values of $c_{x10n}^{1/2}$ computed using Equation (5).

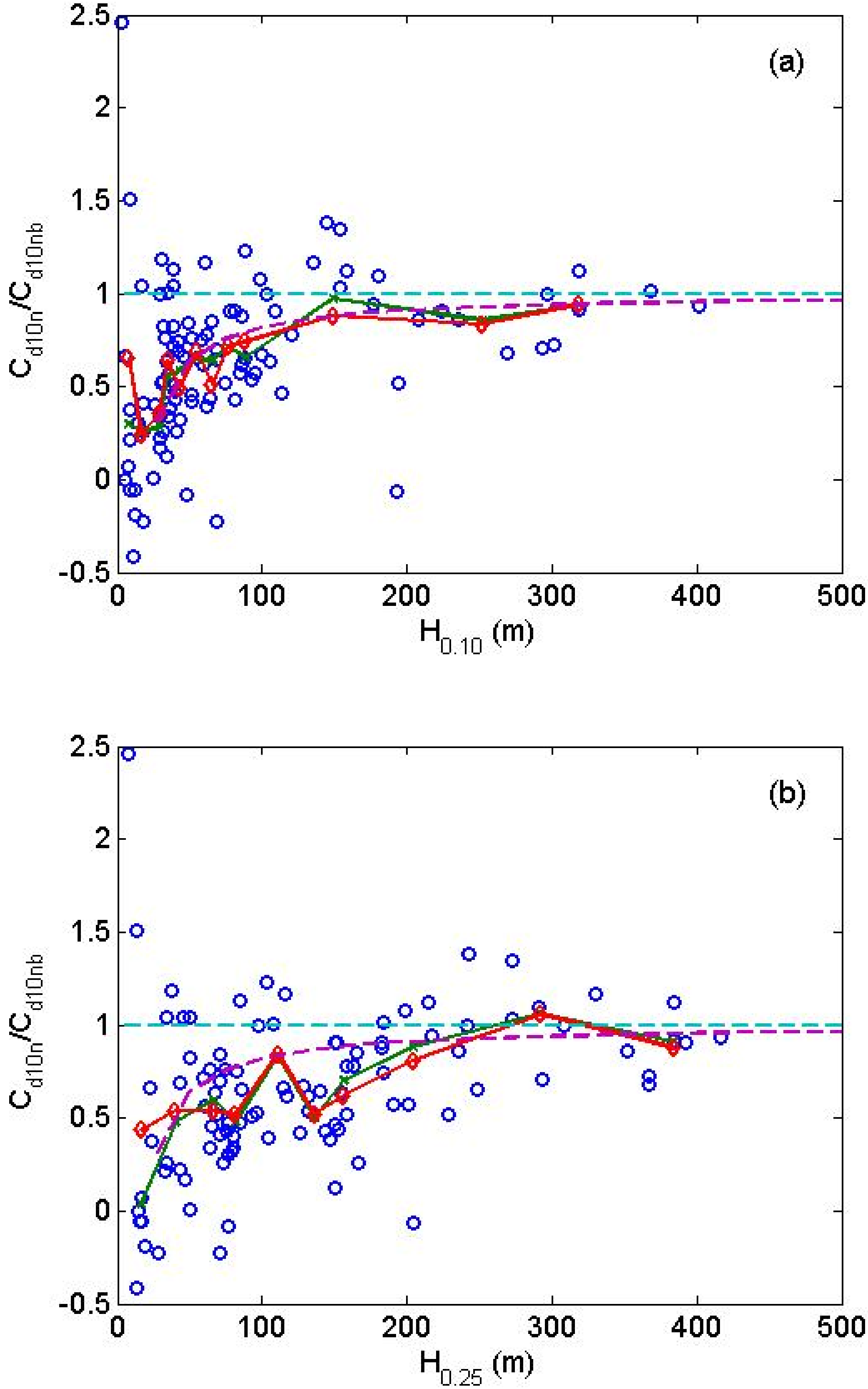
(a)
(b)
C_d10n/C_d10nb
H_0.10 (m)
H_0.25 (m)
2.5
2
1.5
1
0.5
0
-0.5
0
100
200
300
400
500

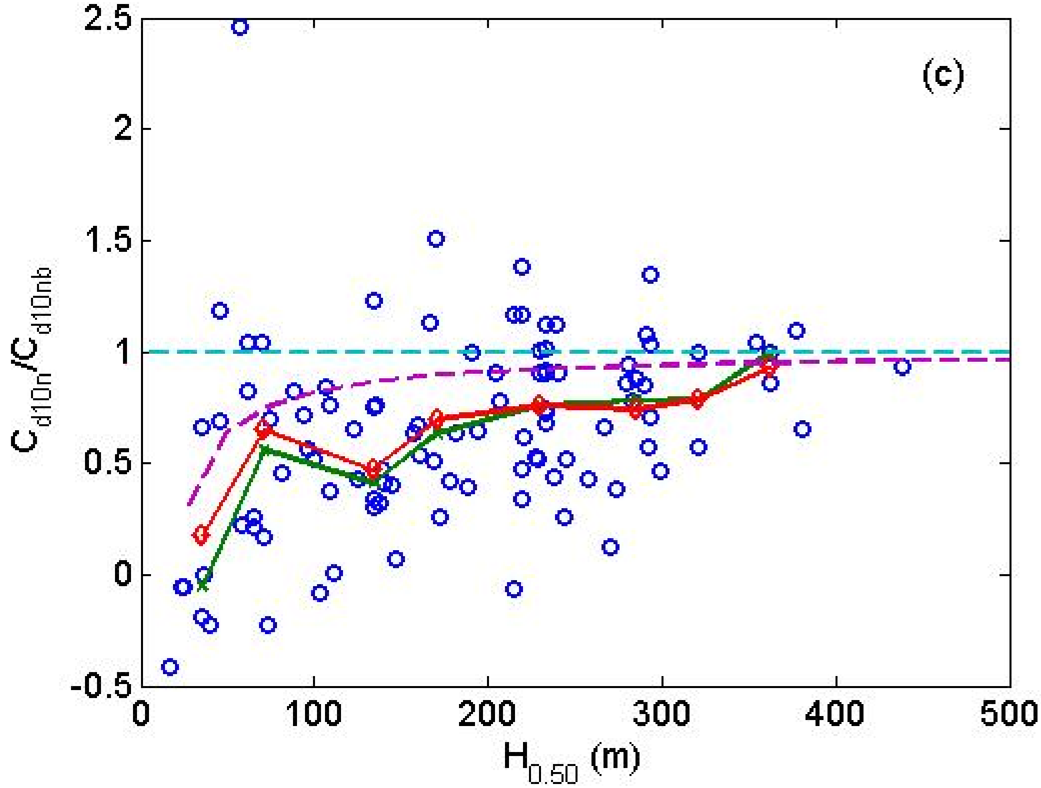

Figure 9. The ratio of measured 10-m neutral momentum transfer coefficient to values for the open ocean (COARE3.0) as a function of boundary-layer depth: circles are the individual 1-hr values, x's are medians, diamonds are means, and the thick dashed line is using Equation (13). Different panels are for different $R_{ib}(z)$ threshold values to define H: (a) Ri_b =0.10, (b) Ri_b =0.25, and (c) Ri_b =0.50.

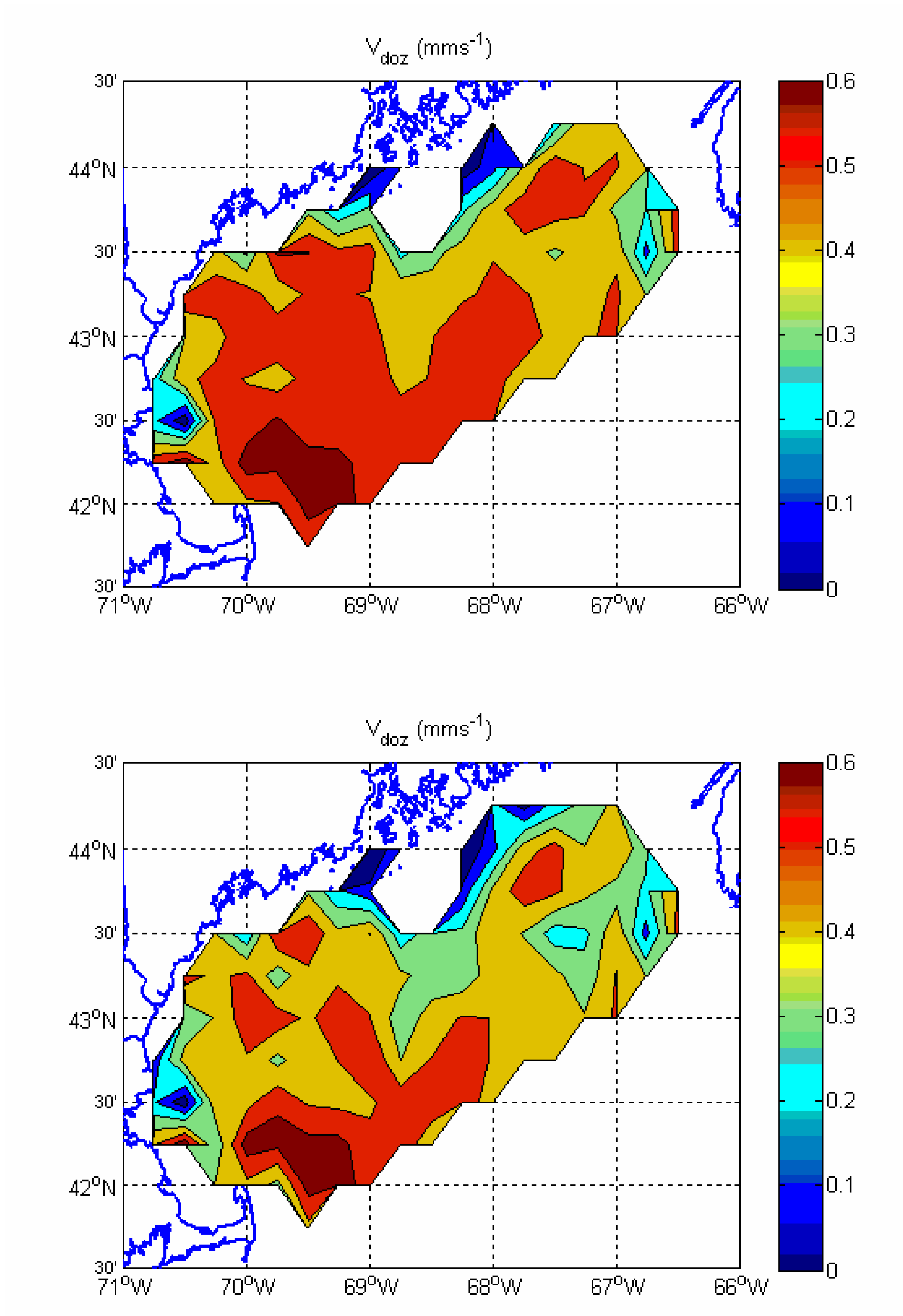

Figure 10. Contour plot of the Ozone deposition velocity using the model of *Fairall et al.* [2006]: upper panel, u_* from COARE3.0 and lower panel, u_* from direct measurement.